Cluster Curlometry Limitations in the Ring Current Region

Timothy B Keebler[1], Michael Liemohn[1,1], Timothy B Keebler[1], and Natalia Ganushkina[2]

[1]University of Michigan
[2]University of Michigan,Finnish Meteorological Institute

December 1, 2022

Abstract

During its ongoing mission, the Cluster II constellation has provided the first small-scale multipoint measurements of the space environment, and dramatically advanced scientific understanding in numerous regimes. One such region is the Earth's inner magnetospheric ring current, which could now be computed using the curl of the magnetic field over a spacecraft tetrahedron instead of via plasma moments. While this produced the first 3D current estimates, it also produced different results from prior ring current studies with differing magnitudes and correlations with storm indices/local times. In this analysis, we revisit Cluster ring current data via curlometry, and conduct additional quantitative sensitivity simulations using actual spacecraft position data. During the orbits that observed ring current structure, tetrahedron shape and linearity assumptions can create large errors up to 100% of physical current magnitude in curlometer output that contradict accepted estimated quality parameters. These false currents are directly related to the structure of the current environment, and cannot be distinguished from the actual currents without additional limiting assumptions. The trustworthiness of curlometer output in the ring current is therefore dependent on the linearity of the magnetic structure relative to the tetrahedron orientation, which requires additional characterization. The Cluster curlometer output in the ring current is then explored in light of these new uncertainties, with the computed current magnitude and direction both potentially impacted by the production of false currents.

Hosted file

`2020ja027914-ms02.gif` available at https://authorea.com/users/560756/articles/608615-cluster-curlometry-limitations-in-the-ring-current-region

Hosted file

`2020ja027914-ms01.gif` available at https://authorea.com/users/560756/articles/608615-cluster-curlometry-limitations-in-the-ring-current-region

Cluster Curlometry Limitations in the Ring Current Region

T. B. Keebler[1], M. W. Liemohn[1], N. Y. Ganushkina[1,2]

[1] Department of Climate and Space Sciences and Engineering, University of Michigan, Ann Arbor, MI.

[2] Space Research and Observation Technologies, Space and Earth Observation Centre, Finnish Meteorological Institute, Helsinki, Finland

Corresponding author: Timothy Keebler (tkeebler@umich.edu)

In preparation for/Submitted to Journal of Geophysical Research Space Physics

Key Points:

- Examination of Cluster curlometer output shows strong evidence of contamination by linearization errors in the ring current region.
- False currents are computed by the curlometer when a large tetrahedron dimension aligns with the magnetic gradient.
- The curlometer technique has highly constrained utility in the inner magnetosphere that requires careful consideration of limitations.

AGU Index Terms:

- 2730 Magnetosphere: inner
- 2778 Ring current
- 2794 Instruments and techniques
- 7833 Mathematical and numerical techniques (0500, 3200)

Keywords:

Ring Current, Cluster II, Curlometer

Abstract

During its ongoing mission, the Cluster II constellation has provided the first small-scale multipoint measurements of the space environment, and dramatically advanced scientific understanding in numerous regimes. One such region is the Earth's inner magnetospheric ring current, which could now be computed using the curl of the magnetic field over a spacecraft tetrahedron instead of via plasma moments. While this produced the first 3D current estimates, it also produced different results from prior ring current studies with differing magnitudes and correlations with storm indices/local times. In this analysis, we revisit Cluster ring current data via curlometry, and conduct additional quantitative sensitivity simulations using actual spacecraft position data. During the orbits that observed ring current structure, tetrahedron shape and linearity assumptions can create large errors up to 100% of physical current magnitude in curlometer output that contradict accepted estimated quality parameters. These false currents are directly related to the structure of the current environment, and cannot be distinguished from the actual currents without additional limiting assumptions. The trustworthiness of curlometer output in the ring current is therefore dependent on the linearity of the magnetic structure relative to the tetrahedron orientation, which requires additional characterization. The Cluster curlometer output in the ring current is then explored in light of these new uncertainties, with the computed current magnitude and direction both potentially impacted by the production of false currents.

Plain Language Summary

The ring current is a structure in near-Earth space that causes magnetic changes on the Earth's surface and is very important for plasma transport as well. Previously, it has been measured using single spacecraft by sampling the electrically charged particles. However, the Cluster mission allowed the ring current to be calculated in greater detail by observing magnetic fields, which are easier to measure. This technique was dubbed the 'curlometer,' and has applications in many regions. For the ring current region in particular, the curlometer technique produces very different ring current strengths than the particle-measurement methods. To resolve this, we reevaluated the curlometer technique and tested it against simulated data for which the current can be analytically calculated, showing larger uncertainty than previously thought. Thus, the curlometer has limitations for using the Cluster mission to measure the ring current.

1. Introduction

The Cluster II multi-spacecraft mission, launched in 2000, has been a resounding success in probing a multitude of environments by collecting data in varying three-dimensional configurations. By providing multipoint measurements, Cluster benefits from improved calibration and novel techniques that cannot be implemented by a single spacecraft (Paschmann & Daly, 2000). One such technique has been named the 'curlometer,' because it uses the four spacecraft as vertices of a tetrahedron to compute the linearized gradient of magnetic field and find the average current density in the tetrahedron volume (Dunlop et al., 1988). Although requiring limitations and assumptions, the curlometer technique has been applied to many regions containing magnetic structure that has a larger characteristic scale than the tetrahedron (Dunlop et al., 2016). Thus, we have gained additional insight into the three-dimensional current structure of features from the cusp to the magnetotail (e.g., Henderson et al., 2008; Dunlop et al., 2015; Petrukovich et al., 2014).

In the ring current region of the inner magnetosphere (~3-7 R_E) (e.g., see reviews and references by Ganushkina et al., 2018, and Dandouras et al., 2018), the curlometer technique has been applied to provide a better estimate of ring current magnitudes critical for understanding storm indices and current closure, also qualitatively capturing field-aligned currents in this region (Vallat et al., 2005; Zhang et al., 2011). Curlometry offers an alternative to computing current from plasma pressure moments, which have higher uncertainty through methodology and instrumentation (Dandouras & Barthe, 2011). Pressure moments can also only yield a single component of current orthogonal to the plane defined by the spacecraft trajectory and local magnetic field, whereas curlometry provides the full current vector.

Currents computed from Cluster via curlometry in the ring current region suggest a westward current that varies from near zero to a few tens of nA/m^2. Vallat et al. (2005) found that the magnitude had no correlation with geomagnetic activity indicated by the Disturbance Storm Time (Dst) index (see Figure 16 and Section 7, Vallat et al., 2005), and using subsequent orbits, other papers (Zhang et al., 2011; Grimald et al., 2012; Shen et al., 2014) have built statistical compilations for the ring current using different thresholds for storm/quiet delineation. However, these results are contrary to plasma moment and single spacecraft magnetometer current calculations, which suggest currents approaching 10 nA/m^2 occur only near storm-times, and are consistently weaker than this value with lower activity (e.g., Lui et al., 1992; Greenspan & Hamilton, 2000; Jorgensen et al., 2004; Le et al., 2004). Furthermore, time series or radial plots of curlometer output (i.e., Vallat et al., 2005) often show structure that is inconsistent with expectations; namely, near-constant current magnitude instead of an inverse relation with L-shell (assuming the pressure peak is radially inward of perigee). These discrepancies urge a thorough reanalysis of Cluster data to account for these observational differences and to probe the underlying assumptions of current calculation (Liemohn et al., 2016). Herein, an approach to curlometry that is mindful of limitations caused by tetrahedron geometry and alignment is developed to characterize the curlometer technique's ability to reproduce known current systems. We assess the Cluster tetrahedron configurations near perigee relative to imposed idealized current sheets, examining the resulting current densities obtained from linear curlometry calculations. Through simulation, the conditions that cause the curlometer to produce false currents are quantitatively characterized, adding a better understanding of the uncertainties associated with these ring current measurements. Through simulation, the conditions that cause the curlometer to produce false currents are quantitatively characterized, adding a better understanding of the uncertainties associated with these ring current measurements.

2. Methodology

2.1. Implementation of the Curlometer Technique

The curlometer technique has been well-documented in numerous papers (e.g., Dunlop et al., 1988; Robert et al., 1998; Vallat et al., 2005); thus, only a brief discussion is provided here. According to the Maxwell-Ampere Law, and assuming stationarity (removal of time dependence term):

$$\mu_0 \vec{J} = \nabla \times \vec{B} \qquad (1)$$

which can be rewritten with respect to a reference magnetic field vector at a reference location:

$$\vec{J} \cdot \left(\left(\vec{r}_i - \vec{r}_{ref} \right) \times \left(\vec{r}_j - \vec{r}_{ref} \right) \right) = \frac{1}{\mu_0} \left(\left(\vec{B}_i - \vec{B}_{ref} \right) \cdot \left(\vec{r}_j - \vec{r}_{ref} \right) - \left(\vec{B}_j - \vec{B}_{ref} \right) \cdot \left(\vec{r}_i - \vec{r}_{ref} \right) \right) \qquad (2)$$

With four spacecraft, the curl of the magnetic field can be computed by cyclically differencing over each face of the tetrahedron to find the three-dimensional linear gradients and summing (Equation 2), yielding the average current density within the tetrahedron volume. Note that in

Equation 2, 'r' denotes the spacecraft position vector, the 'ref' subscript refers to the reference spacecraft, and the 'i' and 'j' subscripts are iterated through non-reference spacecraft pairs. A more detailed treatment of the technique can be found in Dunlop et al. (1988) or Middleton and Masson (2016).

For this study, the curlometer computation was performed by modifying a Python script provided by the Cluster Science Archive (CSA) (http://www.cosmos.esa.int/web/csa/multi-spacecraft/). The script was thoroughly tested for correct methodology: first with sample data provided by CSA, then by alternating reference spacecraft and perturbing parameters, and finally by 'flying' the constellation through simulated linear current environments. In each case, the output was as expected, demonstrating independence of reference spacecraft choice and correctly capturing the simulated currents. This analysis followed the work of Robert et al. (1998) and independently confirmed the results of that study. The code was further verified by replacing magnetic field data with constant field, correctly producing no current, with an idealized dipole field, producing small current (< 2 nA/m^2) due to nonlinear magnetic gradients, and with the International Geomagnetic Reference Field (IGRF) (Alken et al., 2021), which also created only small current outputs (< 3 nA/m^2 with 2002 tetrahedra) as expected (Dunlop et al., 2020). Thus, the curlometer script was confirmed to function correctly in a variety of environments. A sample of these tests for different tetrahedra is provided in supplemental material. Extensive testing provided the necessary foundation for later conclusions by definitively verifying the curlometer computation.

Magnetic field data from the Fluxgate Magnetometer (FGM) instruments on each spacecraft were obtained in spin resolution along with spacecraft ephemeris data. The resolution of the magnetometer measurement at the observed field strength is roughly 0.125 nT (Balogh et al., 1997); the effect of this resolution was determined to be no more than +/- 2 nA/m^2 in curlometer output in agreement with the analysis done by Vallat et al. (2005), and a sample is provided in supplemental material. For this present study, temporal data resolution was experimentally determined to have only a small effect on current values, within the ranges of available datasets; therefore, spin resolution (~4 s cadence) sufficiently captures the scale of desired features. All values were converted from Geocentric Solar Ecliptic (GSE) to Solar Magnetic (SM) coordinates using the SpacePy Python package (Morley et al., 2011) and tested to ensure they retained their magnitudes. Note that westward azimuthal current is defined to be positive due to convention in prior studies. IGRF values were then subtracted from the magnetic field data to remove as much nonlinear magnetic gradient as possible and therefore allow a more robust linearity assumption and curlometry result (Dunlop et al., 2016; Dunlop et al., 2020). This has a significant effect on current densities for spacecraft separations above 200 km.

2.2. Ring Current Event Selection

During the period of study for this analysis, the Cluster spacecraft operated in highly-elliptical orbits with perigee of ~4 R_E, apogee of ~20 R_E, inclination of ~90°, and period of ~57 hours. The spacecraft flew in various evolving formations that had interspacecraft separations less than 1000 km. The Cluster tetrahedron was most regular within the ring current region for select dates from 2001-2004, which is critical for accurate curlometer output. Using prior studies for guidance in event selection (Vallat et al., 2005; Zhang et al., 2011; Shen et al., 2014), six hours of data surrounding every perigee pass individually underwent visual inspection. Each pass was run through the curlometer script and examined. Perigee passes were removed if data was missing from anywhere in the expected ring current region, or if there were obvious errors in the data (e.g., discontinuities, asymptotes). This filtering of missing data therefore removed passes that experienced eclipses.

Figure 1 presents an example of the Cluster data examined for this study, specifically from the 9 May 2002 perigee pass, when the tetrahedron shape was within the nominal guidelines for yielding reasonable current densities from the curlometer technique. The tetrahedron characteristic size was just under 200 kilometers, with the largest separation at about 250 kilometers. This pass has a minimum radial distance of 4.3 R_E and a magnetic local time near 20:00. The timeseries shown is from south to north, maintaining the magnetic local time near 20:00 with only small deviations from meridional motion. The magnetic equator is at approximately 18:20 UTC, with Southern Hemisphere observations prior to that time and Northern Hemisphere observations subsequently. The top two panels show the current density computed from the curlomter Python script, first in SM coordinates (Figure 1a) and then just the azimuthal component (Figure 1b). In Figure 1a, the total current magnitude is plotted in the black line, while colored lines are Cartesian current components. Figure 1c shows the interspacecraft differences in magnetic field magnitude used in the curlometer calculation. Spacecraft geometric parameters, tetrathedron quality, and radial current are also plotted for reference in the supplemental material. The vertical red dashed lines roughly outline the region of interest, as marked by smooth curlometer output.

Several features are readily seen in Figure 1. First, there is a smooth section of current around the magnetic equator, surrounded by intervals with highly fluctuating currents. Second, the magnetic field differences do not show a drastic change at the variable/smooth boundary (the red-dashed vertical lines). That is, the current densities come from rather small deviations in magnetic field differences, sometimes hardly noticeable on the plotted scales. The perturbations in the magnetic field that cause large oscillations in the current are very small, less than 0.1 nT, and the differences across the tetrahedron (Figure 1c) that are used for computing current are far smaller than the typical field strength at this distance of about 400 nT. Also note an apparent symmetry in the azimuthal current along the trajectory, as expected.

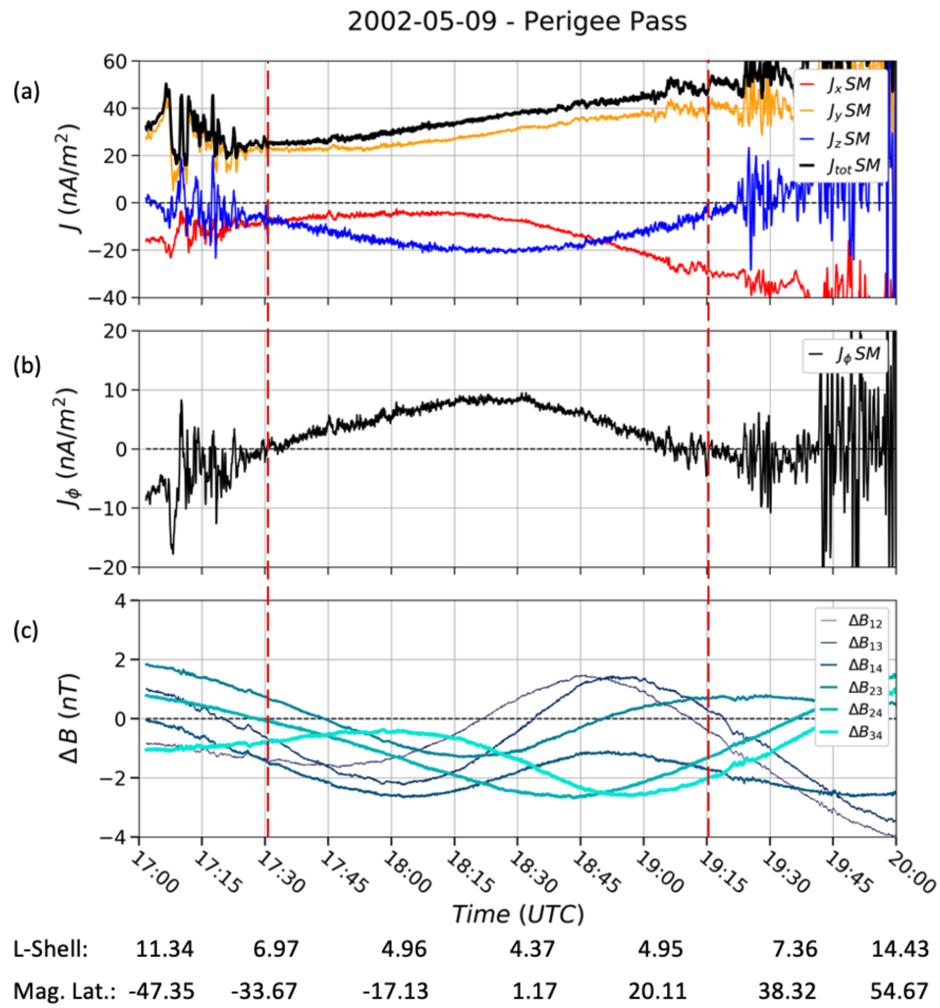

Figure 1. 9 May 2002 Perigee Pass Timeseries. The satellite constellation is flying south to north at approximately 20:00 magnetic local time. **a)** Curlometer current components in SM coordinates. The black line is the total current magnitude. **b)** Azimuthal current component (J_ϕ) in SM coordinates. **c)** Inter-spacecraft magnetic field differences. Dashed vertical lines delineate the region of interest. L-shell values are provided every 30 minutes.

Similarly to the example in Figure 1, all perigee passes were examined to capture and identify the region of interest as the area with smooth current profile. Outside the region of smooth current signatures (outside red dashed lines), curlometry yields wildly oscillating current components as a result of the complex structure in these regions below the tetrahedron scale size (Vallat et al., 2005). Conversely, the presumed ring current section of the orbit is marked by a smooth timeseries indicating a homogeneous structure. After identification, the set of all cases was then used to demonstrate the uncertainties detailed herein.

2.3. Nonlinear Current Simulations and Tetrahedron Shape

To investigate the performance of the curlometer in different environments, simplified simulations were used to probe for possible error. When testing curlometry through simulated magnetic fields, deviation from linear magnetic gradient causes errors in the output current. Robert et al. (1998) suggests that this effect is <10% for a regular tetrahedron with elongation and planarity both below 0.8 (see Paschmann & Daly (1998), Chapter 13, for detailed treatment of tetrahedron geometric parameters). Defined as the ratio between magnetic divergence and magnetic curl, the quality parameter $Q = |\mathrm{div}(B)|/|\mathrm{curl}(B)|$ has also been used to determine regions where the curlometer has better performance, with $Q = 0.5$ as the standard threshold (e.g., Dunlop et al., 1988, Vallat et al., 2005, Zhang et al., 2011). However, a comparison between idealized current as input and curlometer output has not been conducted using actual spacecraft position data. This process is distantly similar to that of Dunlop et. al (2002), but uses a more idealized situation and a more focused region of interest.

To represent the simulated currents, an infinite planar current sheet was constructed with thickness scaled to the selected perigee pass and quadratic variation from 0 nA/m^2 at the boundaries to 10 nA/m^2 at the center; the simulated current sheet was then offset to the center of the selected spacecraft flight track. Although greatly oversimplified, this model creates gradients consistent with structural understanding of the magnetosphere (eg. Le et al., 2004) and of similar magnitude as proposed by Vallat et al. (2005). Using the Biot-Savart law, the magnetic field vectors were computed at each spacecraft location, then passed through the curlometer script. A simplified visualization is provided in Figure 2, depicting the spacecraft trajectory, variation of current, and magnetic field for a single case. Figure 2a shows the current density constructed for the simulated system in blue; the corresponding magnetic field generated by this current is in Figure 2b in black. Finally, Figure 2c shows another representation of the current density as blue shading, magnetic field as black arrows, and a cartoon Cluster constellation flying through the simulated environment from bottom to top in red.

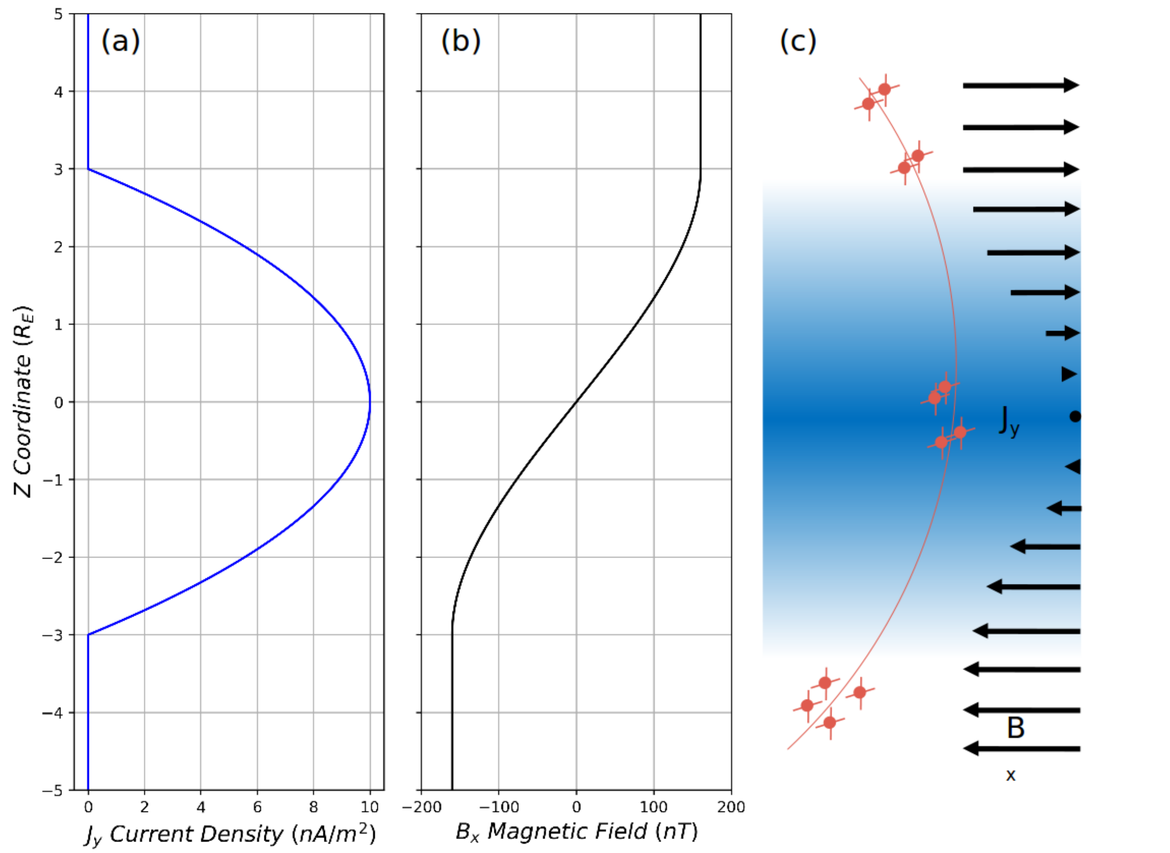

Figure 2. Simulated Current System. **a)** Slice through simulated current sheet, in nA/m^2, of the J_y current component (blue). This plot is the current experienced by a Cluster spacecraft as it flies through the simulated environment. **b)** Magnetic field corresponding to the simulated current (black). These values replace the measured magnetic field from the Cluster spacecraft for simulation purposes. **c)** Alternate visualization of simulated environment. Black arrows denote magnetic field from (b). Blue shading indicates quadratically-varying current density from (a). Simplified spacecraft flight track and tetrahedron evolution are shown in umber.

Because the Cluster tetrahedron had some degree of irregularity in shape near perigee on all orbits, the simulated current sheets were iterated through all orientations and current directions. In other words, the simulated current sheets were constructed in each component direction, J_x, J_y, and J_z, and also with the current sheet normal direction varied for each case. Additionally, for each current sheet orientation, the tetrahedron was rotated about the barycenter by way of individual spacecraft positions and reanalyzed to deduce the combined effect of current direction and tetrahedron aspect. Thus, the possible geometric combinations of the simulated current and tetrahedron were completely explored for the ring current environment as observed by Cluster.

3. Results

As discussed in the methodology section above, idealized current configurations were used to replace the observed Cluster magnetometer data with simulated data, for which the corresponding current density is known. Figure 3 shows the results of an idealized current sheet in the J_y direction centered in the z = 0 plane. The current density varies quadratically from J = 0 at the boundaries to a maximum in the center of 10 nA/m^2 with a total thickness of 5 R_E. This thickness was based on the observed ring current thickness of the selected event. The tetrahedron was 'flown through' the simulation using actual position data from 10 October 2003 (other events provided in supplemental materials) and replacing the magnetic field with values computed from the simulated current sheet using the Biot-Savart law (Figures 3a-3c). Figure 3a shows the calculated currents from the original unrotated tetrahedron, with the imposed currents represented by dashed lines and the calculated currents represented by solid lines. The green lines are the J_y component, which is the imposed component that is expected to be captured. The blue lines are the J_z component, which is set to 0 in the imposed current and expected to be computed as 0 as well. Figure 3b contains the corresponding quality parameter Q. The boundaries of the threshold Q = 0.5 are marked with vertical red dashed lines. In Figure 3c, the locations of all spacecraft relative to the constellation barycenter are plotted as the vertices of the tetrahedron, to visualize the constellation shape. Figure 3c also contains arrows to show relevant vector directions, including current direction (black arrow), magnetic gradient (blue arrow), and longest planar axis (red arrow). Note that the planarity vector shows the direction of the largest semiaxis, instead of the planarity normal direction. The tetrahedron was then rotated about its barycenter around the x-axis by 90° to produce Figures 3d-3f. Figure 3d shows the currents as in Figure 3a, Figure 3e shows the Q calculation as in Figure 3b, and Figure 3f shows the constellation as in Figure 3c, following the 90° rotation.

It is immediately apparent that, despite the simulated current being purely in the J_y direction, a large false current is output by the curlometer technique because of the non-zero J_z current. In this instance, the false current grew as large as 5 nA/m^2 in the J_z direction (solid blue line, Figure 3a). The unaltered tetrahedron orientation produced nearly the greatest false currents of any rotation direction. Furthermore, the large false currents occur well below the Q < 0.5 quality standard in Figure 3b, with significant stature even at more stringent thresholds. In other words, the false currents occur between the red dashed lines denoting acceptable curlometer quality. Rotating the tetrahedron about its barycenter, however, produced different results (Figure 3d). Instead of a large false current, the same tetrahedron parameters with a quarter rotation captured the currents remarkably well with little deviation between dashed and solid lines (Figure 3d), and Q is much lower throughout the pass (Figure 3e). All else equal, rotation dramatically changed the output by altering the planar direction with respect to the magnetic field gradient. When rotated farther, currents appear again, related to the orientation of magnetic gradient with respect to planar direction. An animation of rotating the tetrahedron with corresponding curlometer output is provided in supplemental materials. Larger false currents are produced when the largest planar semiaxis is more parallel to the magnetic gradient; this can be seen by comparing the red and blue arrows in Figures 3c and 3f. During analysis, the tetrahedron was rotated independently and in combination of all three axes, with only the extrema of false currents highlighted in the figure. Rotation about other axes produced smaller false currents, so the uncertainty contributions from those axes are smaller. False currents are directly related to the length of the tetrahedron semiaxis parallel to the magnetic gradient; therefore, some rotations will roughly preserve that quantity.

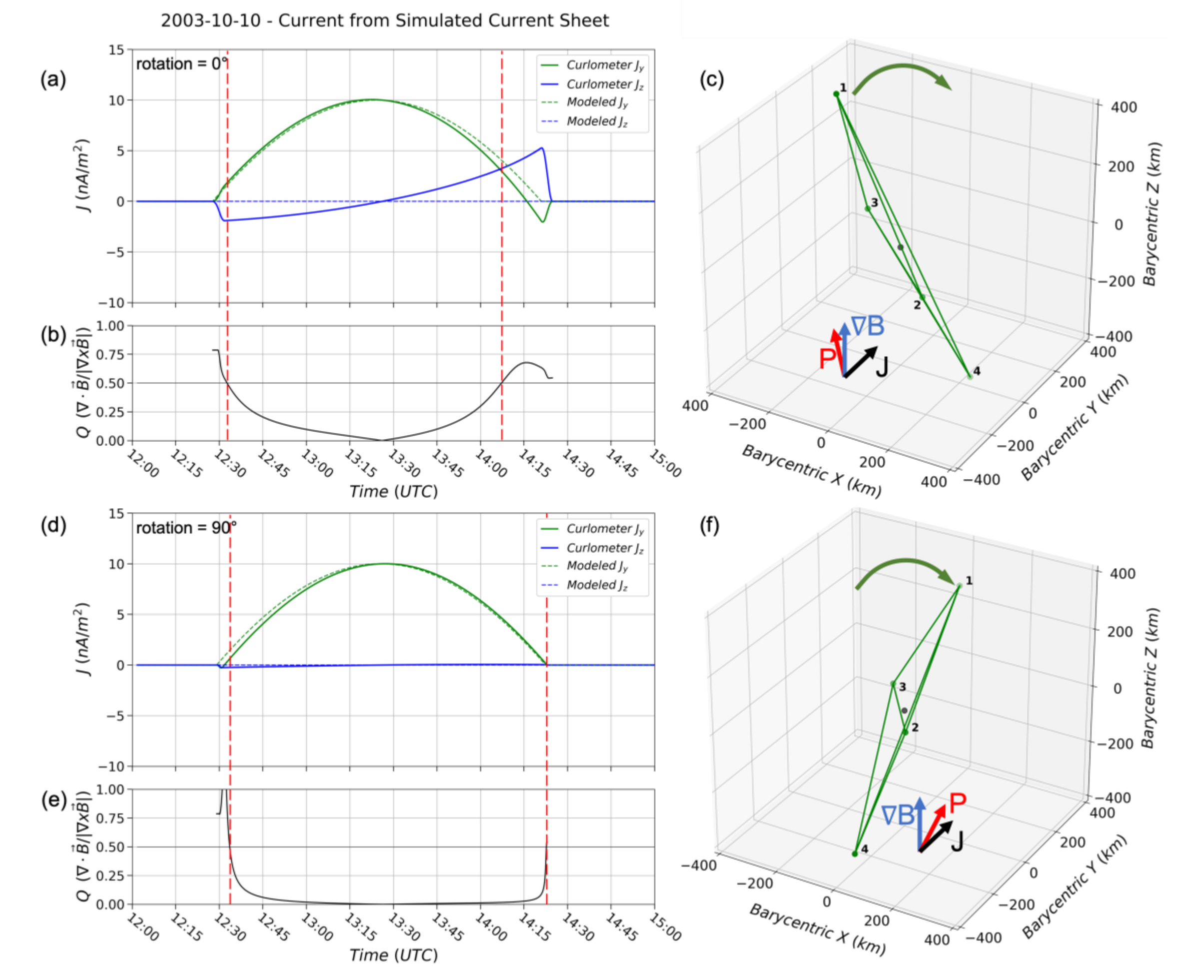

Figure 3. Quadratically varying infinite current sheet centered on the z=0 plane using the orbit spatial parameters from 10 October 2003. From unaltered flight track position data: **a)** Curlometer output (bold) and imposed simulation current (dashed). **b)** Quality parameter Q. **c)** Tetrahedron shape and environment vectors. For **d)** - **f)**, the current sheet remained the same, but the tetrahedron was rotated about the barycenter by 90°, pivoting clockwise around the x-axis. Red dashed lines denote the region with Q < 0.5. In (c) and (f), the black arrow 'J' depicts the direction of simulated current. The blue arrow '∇B' shows the gradient of magnetic field. The red arrow 'P' shows the orientation of the longest tetrahedron semiaxis.

Using simulated currents and tetrahedron rotations like those that produced Figure 3, the curlometer calculation yielded large non-physical currents in complementary components with different simulated current directions and tetrahedron rotation axes as well. Despite this example emphasizing the production of J_z, gradients in other directions do impact the azimuthal current in the same way. Thus, without a priori knowledge of the environment, false currents may appear in any direction depending on the gradients present. These false currents are in the direction of the magnetic gradient associated with the magnetospheric current sheet (like the spurious J_z in Figure 3a), but the magnitude was highly dependent on tetrahedron orientation and shape parameters. Even in regions where Q < 0.5 for the curlometer computation, false currents could be as much as 100% of the imposed current at a given time (5 nA/m^2 of J_z created by 5 nA/m^2 of J_y), with significant implications that ring current curlometry can be highly inaccurate despite accepted data filtering methods.

Rotating the tetrahedron about the barycenter provided additional insight into the relationship between shape, orientation, and false current. Elongation was consistently near 0.8 for all passes and timestamps, but planarity evolved quickly from 0.4 to near unity in the few hours surrounding perigee. Thus, planarity was observed to have the larger effect of the shape parameters in these flight tracks, and maximum false current was produced by the largest planarity semiaxis that was close to being parallel to ∇B and therefore experiencing the largest linearization error. In cases with multiple gradients, false and physical currents added linearly through the curlometer, requiring understanding of physical currents to deduce the false components. However, false current was also strongly related to nonlinearity in magnetic gradient, so without quantitative knowledge of this it is impossible to correct in-situ data for these differences. Numeric correction of curlometer output requires additional study and technique development and will be severely limited by enhanced stationarity assumptions.

4. Application to Cluster Data

Considering the production of false currents in the simulated environment, this section provides an initial view of the Cluster ring current observations in the context of increased uncertainty. The application of the curlometer technique to this dataset produces current structures that are consistent with nonlinearity current artifacts as seen in the simulated currents.

4.1. Representative Curlometry

Previously in this study and others (e.g., Vallat et al., 2005, Zhang et al., 2011), the quantity Q = div(B)/curl(B) was used as a quality flag, with values less than 0.5 considered acceptable uncertainty. However, simulated currents can produce false results with the same order of magnitude as the imposed currents even when Q is below the 0.5 threshold (as seen in Figure 3), depending on tetrahedron orientation. Orbits in the Cluster dataset each only contain a small duration under this threshold and are likely to contain larger magnitude errors outside this range. While the latitudinal extent of the ring current can be established with reasonable confidence via plasma data and regularity of current profile, information regarding the magnitude and direction of the current may be grossly inaccurate. Examining tetrahedron orientation through simulated current sheets produced new maximum uncertainty estimates that exceed the elongation-planarity plots constructed by Robert et al. (1998), which suggest current magnitude errors rarely exceed a mere 10% when both elongation and planarity are below 0.8 (see, for example, Figures 16.7 and 16.8 in Robert et al., 1998).

New selection criteria for suitable ring current data must examine the curlometer output in conjunction with the quality parameter Q and a priori knowledge of the magnetospheric environment to judge data validity. Only data with a maximum Q of 0.5 should be considered in climatological studies of the ring current because instances above this threshold almost certainly have large errors in both magnitude and direction. Lowering the threshold further increases confidence, but at the expense of sample size. To effectively filter curlometry output, a more complete analysis of tetrahedron and environmental parameters needs to be constructed, both through higher-degree estimates of nonlinear magnetic field gradient and the orientation with respect to the tetrahedron. Curlometer uncertainties stem not only from tetrahedron geometry, but from the geometry in combination with the magnetic environment. Then, additional quality standards can be developed to increase trustworthiness of current calculation at the expense of the resolution.

4.2. Single-Event Current Features

Figure 4 provides a representative sample of a single perigee pass, from 10 October 2003. This is the actual curlometer calculation from magnetometer observations, in contrast to the simulation in Figure 3. While the observed current structures varied widely across the total dataset, this event provides a typical case that shows common trends and avoids extremes. It is important to note that the tetrahedron characteristic size varies greatly between data from 2001, 2002, and 2003-04 flight configurations. Thus, the example chosen in Figure 4 represents the most observations but not necessarily the best. As in Figure 1, the spacecraft are traversing the inner magnetosphere from the Southern Hemisphere to the Northern Hemisphere with only small meridional deviation. The magnetic equator is crossed near 13:00 UTC, and this pass is located at local time 09:40. Figure 4a shows curlometer output in SM Cartesian current components, with the components clearly diverging later in the timeseries. The total current magnitude is plotted in black. Figure 4b displays the azimuthal current component computed from the Cartesian components. These current values are then compared to the quality parameter Q = div(B)/curl(B) in Figure 4c and the tetrahedron geometry in the form of elongation (red) and planarity (blue) in Figure 4d. Note that the geometrics are plotted on separate y-axes in Figure 4d to capture detail. The plot limit times have been chosen to fully enclose spacecraft perigee by several hours and with the "smooth" sections used as a means for identifying the region of interest.

For this inner-magnetospheric traversal, a few key features immediately stand out. The Cartesian current components quickly diverge near the end of the selected data (Figure 4a), which in turn causes the azimuthal current component to develop a strong negative trend (Figure 4b). Figure 4b shows an environment where the azimuthal current is westward in the Southern Hemisphere before decreasing to 0 just north of the magnetic equator and becoming eastward into the Northern Hemisphere. This is clearly nonphysical behavior, and cannot be trusted to accurately represent the ring current. Given the south-to-north trajectory, the azimuthal current should vary with radial distance/L-shell, not with latitude as seen here. Instead, the curlometer-derived current topology in Figure 4 looks very similar to the simulated environment in Figure 3, suggesting false currents are to blame for the divergence. The large uncertainty in the data is corroborated by the calculation of Q, which is only below the standard threshold of 0.5 in the beginning of the flight track (Figure 4c). However, even during periods of relatively high confidence, the currents are still diving towards negative values. A potential explanation for the diverging current lies in the tetrahedron geometry (Figure 4d), which has a high elongation ($E > 0.8$) and an increasing planarity (from $P < 0.4$ to $P = 1$) where low values are more regular and desirable. These extreme geometric factors produce false currents as in Section 3.

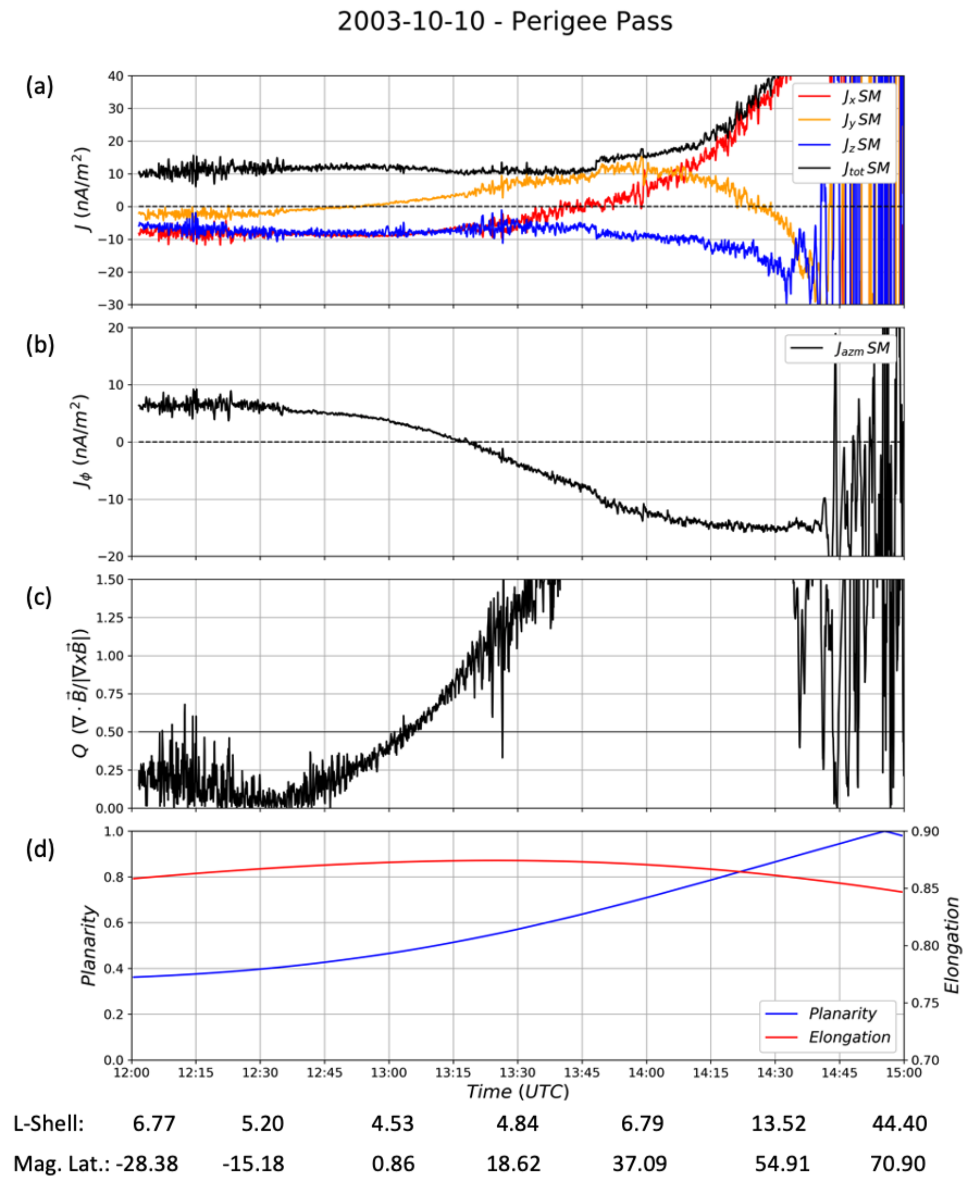

Figure 4. 10 October 2003 Perigee Pass. The satellite constellation is flying south to north at approximately 09:40 magnetic local time. **a)** Cartesian current components in SM coordinates, showing clear divergence after perigee. Total current magnitude is shown in black. **b)** Azimuthal current density J_ϕ. **c)** Quality parameter Q, satisfying the Q < 0.5 threshold until just after 13:00. This is not centered on the ring current region. **d)** Tetrahedron shape parameters elongation and planarity. Note that planarity is steadily increasing to unity throughout the ring current traversal, and that the axes scale differently.

In all orbits where Cluster achieved relatively regular tetrahedra when traversing the ring current region, curlometry results varied greatly in structure and magnitude. Nearly all passes had azimuthal current components in a westward direction with a magnitude peaking at or below 10 nA/m^2. Many perigee passes also featured similar azimuthal current profiles to the one on 10 October 2003 in Figure 4. This is inconsistent with our understanding of physical current structures (e.g., Ganushkina et al., 2018), and calls the curlometer result for these diverging regions into serious doubt. Data from 2003-2004 is especially susceptible to the decrease and reversal of azimuthal current in similar fashion to Figure 4b, especially in regions where the tetrahedron evolves to higher planarity. While the azimuthal current never becomes negative while Q < 0.5, it does begin to decrease towards zero within this criterion.

Curlometer output also showed large cross-hemisphere field-aligned currents (FACs), around 10 nA/m^2 on 10 October 2003. This can be seen in Figure 4a using the J_z component as a proxy for FACs due to magnetic field lines primarily along that axis. The persistence of FACs in the curlometer output for all events will be discussed in more detail in the next section.

4.2. Cluster-Derived Ring Current Environment

If the simulated current environments and the false currents produced in those simulations have any bearing on the actual ring current system, similar effects should appear in curlometer output using the original spacecraft magnetic field observations. To establish a view of the ring current at all local times, it is important to have a large and representative sample of measurements throughout the whole precession of the Cluster orbit. This aim would be hindered by the extensive data filtering required to produce meaningful curlometer results, removing any non-physical results or using an advanced algorithm to determine magnetic gradient nonlinearity. Thus, the holistic plots here are subject only to the restriction on quality parameter Q, and investigated for signs of false current presence despite an accepted quality.

All perigee passes are considered in Figure 5. Taking data with Q < 0.5 and with L < 7 R_E, events were sorted into “disturbed-time” and “quiet-time” categories delineated by Dst = -25 nT. This threshold was set to have a very clear set of “quiet-time” observations, despite placing some nearly-quiet observations into the “disturbed” category. Figure 5a provides curlometer output for disturbed magnetospheric conditions (red data) and for quiet conditions (black data) as a function of L-shell. While disturbed events can show wild variation and sparse data coverage, quiet events provide insight into the radial ring current distribution. The spread of quiet data only is visualized via boxplot in Figure 5b, binned by L-shell in 0.2 R_E increments. Figure 5c shows the number of observed current values in each bin. The majority of ring current observations with Q < 0.5 lie Earthward of L = 5, so conclusions in this region are more robust.

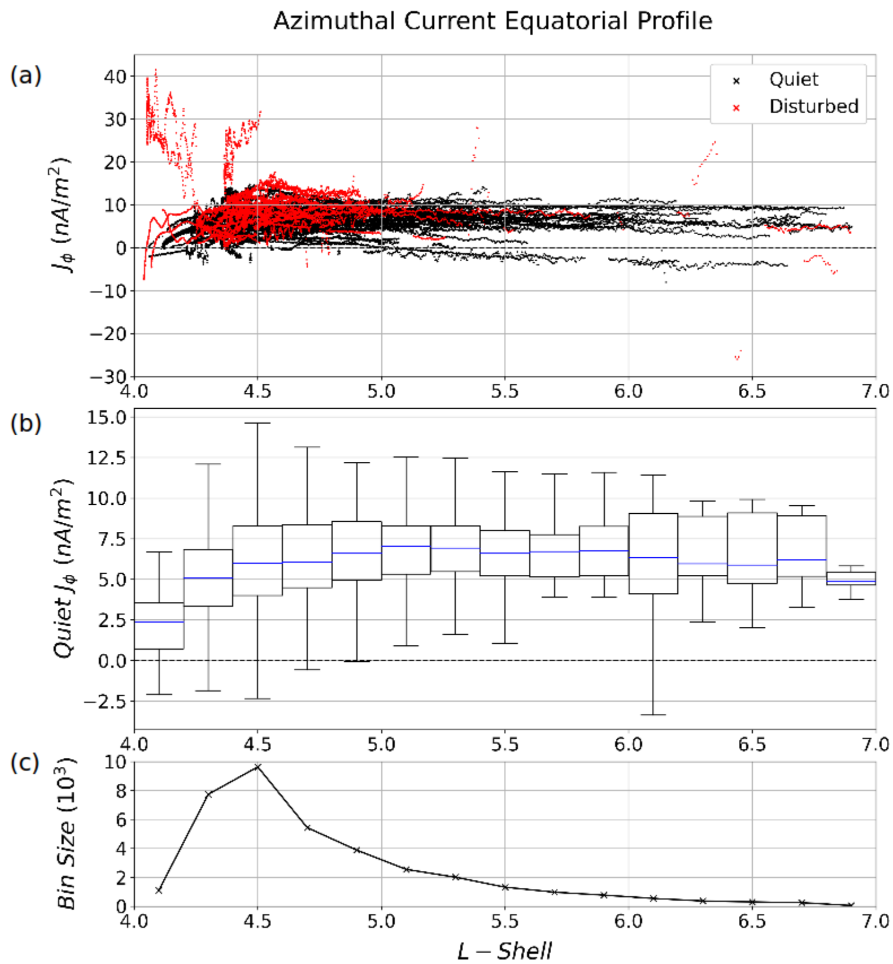

Figure 5. Ring Current Statistical Radial Profile. **a)** Azimuthal current as a function of L-shell. Quiet magnetosphere conditions are shown in black, and disturbed conditions are shown in red. **b)** Quiet-time current distributions. Box heights show the median (blue) and interquartile range (IQR), box widths represent current binning with respect to L value at 0.2 L per bin, and vertical bars indicate values up to 1.5*IQR. **c)** Observation count per data bin.

The ring current as measured by Cluster between 2001 and 2004 was largely below 10 nA/m^2 in magnitude, with a marked decrease towards L = 4 R_E. This suggests that the eastward reversal of the ring current usually lies inside the Cluster orbit and is not observed, although there is less data in this region, and agrees with prior studies (Shen et al., 2014; Vallat et al., 2005). However, at all values of L, the median of ring current magnitudes was below 7.5 nA/m^2, and the third quartile was below 10 nA/m^2, as seen in Figure 5b. This better agrees with plasma pressure calculations but contradicts earlier curlometry, such as the results of Vallat et al. (2005). Additionally, this could still be impacted by up to 2 nA/m^2 of uncertainty from magnetometer resolution, and by the production of false currents. For disturbed magnetospheric conditions, less data were available and the scatterplot reveals higher spread (red data, Figure 5a). The linearization assumption becomes even less robust during geomagnetic activity, because the extent of via viable disturbed-time data is much smaller than quiet-time data (the limiting factor is usually that $Q < 0.5$ for a shorter duration). Nevertheless, the radial profiles of azimuthal current shown in Figure 5 do not show any characteristic signs of contamination by false currents.

Figure 6 visualizes a subset of the full current vectors in 3D space. The data were subjected to the same quality constraint $Q < 0.5$ as before and were then binned and averaged in 15-minute intervals for plotting clarity. The plot contains both disturbed and quiet-time data, and all local times. In this figure the J_z component is strong in most cases, and almost always negative. In fact, the dominant current at most latitudes is southward field-aligned current as indicated by the arrows generally pointing southward. The largest FACs are in excess of 20 nA/m^2 in perigee passes from 2002, and FACs in most other orbits were southward at ~5 nA/m^2 and did not vary significantly between hemispheres. Prior curlometer analyses do not focus on FACs because they are understood to be poorly represented. However, the topological identification of FACs has precedent (e.g., Vallat et al., 2005, Zhang et al., 2011). This is the first report of such large currents in such consistent direction, and should be viewed with extreme caution. The FACs in the inner magnetosphere are not expected to be so persistently in the same cross-equatorial direction at all latitudes and local times. Thus, the large field-aligned component provides evidence that the curlometer output may not be a good representation of the actual currents. A consistent current of this magnitude and direction is characteristic of false currents produced by the curlometer technique under unfavorable magnetic environments. Because of the interconnected nature of curlometer output components, these FACs also call the azimuthal currents computed by curlometry into question. This ubiquity and consistency of a southward FAC, regardless of geomagnetic activity, latitude, or local time, is characteristic of false currents.

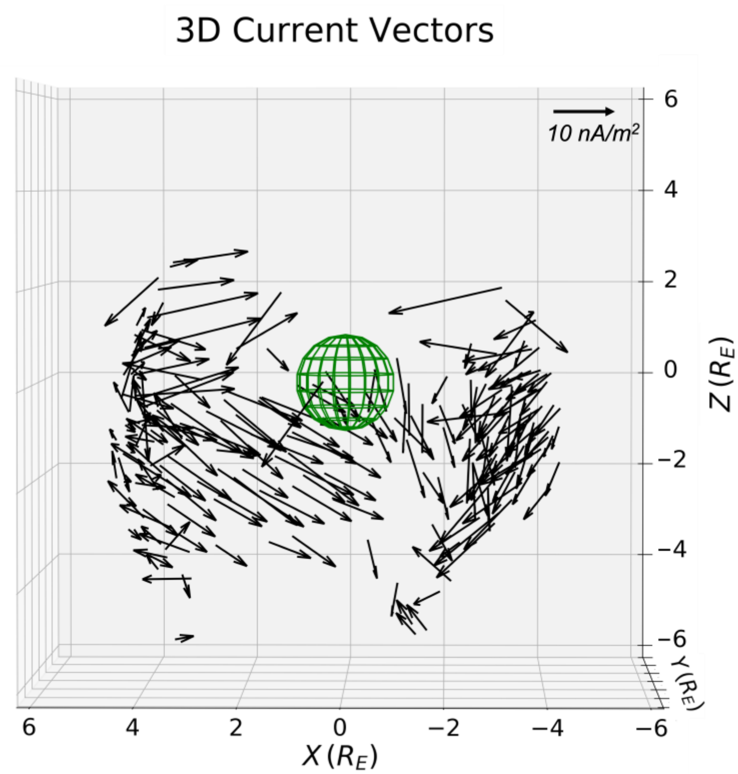

Figure 6: 3D Current Vectors. All perigee passes were included, subject to the constraint of Q < 0.5. Included vectors were binned and averaged over 15-minute intervals to avoid clutter. For a top-down view depicting local time dependence and clearer radial components, see Figure 7.

For further visualization of these non-physical curlometer outputs, currents with Q < 0.5 inside L = 7 (same criteria as Figure 5) were averaged for each perigee pass; the results are provided in Figure 7. Figure 7a shows the full horizontal current vectors, and Figure 7b shows just the azimuthal component. Note the large radial components of current at all local times for nearly all events in Figure 7a; this is not expected quiescent ring current structure (e.g., see review and references by Ganushkina et al., 2018), nor has it been reported in any previous study. Consideration of just the pure azimuthal component (Figure 7b) provides a misleading picture because it omits the strong Earthward components, as well as the z-component as seen in Figure 6. Providing the full current vector or combining azimuthal and radial components adds additional evidence of the presence of false currents by allowing the full complexity of the output currents that lack a plausible physical explanation.

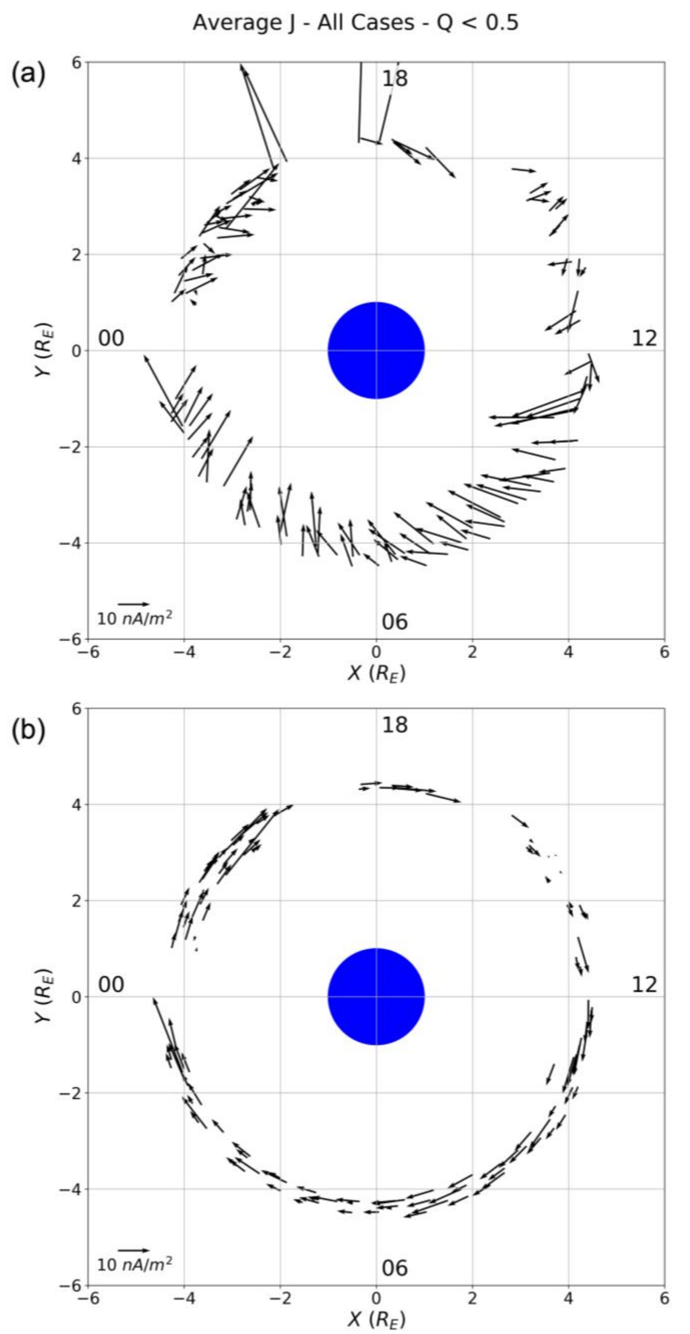

Figure 7. Current vectors averaged by orbit over Q < 0.5 for L < 7. **a)** Full current vectors in the x-y plane. Each vector is averaged about the magnetic equator for clarity. Note that this is a top-down view of Figure 6. **b)** Azimuthal current components of the vectors in (a).

While the above estimates provide methodically-consistent ring current computation, each perigee pass can also be assessed individually to account for signs of nonphysical output in the computed currents. These include the divergent current components as displayed in Figure 4a. Data from 2001 should be discarded because it does not usually show a clear transition to the ring current region, and because the tetrahedron characteristic size is larger than 1000 km. Additionally, data from the 2003-2004 orbits can sometimes be noisy or have large cross-equatorial trends that should be eliminated. Finally, the case from 18 March 2002 should be excluded from holistic analysis because of the uniqueness of the observed current structure. Despite the focus on this event in Vallat et al. (2005), the physical implications for plasma populations and magnetic topology necessitated by a constant and strong ring current through a large swath of the orbit require special case study. However, aggressive removal of non-ideal perigee passes does not alter the persistent large FACs show in Figure 6 and Figure 7, nor the radial profile in Figure 5. This suggests a systematic presence of curlometer errors that are appearing in all cases, regardless of the available filtering criteria.

Considering these structures and the likely reasons for the non-physical currents, Cluster curlometer output is limited for assessing the inner magnetospheric ring current density. There is more information contained in analysis of individual passes than in views of the system as a whole, and qualitative trends provide the most confidence in these cases. It is sufficient to note that the ring current is a highly-variable structure, in both magnitude and extent, and therefore small variations in the environment can lead to drastic changes. Without a definitive way to remove the full 3D effects of false current generation, however, quantitative analysis of ring current Cluster data has significant uncertainty that precludes definitive determination of current densities and orientations.

5. Discussion

The curlometer technique has produced unexpected results in the discussed applications: simulated current environments, single perigee passes, and holistic studies of all available events. In the simulated current environments, the curlometer calculation reproduced the imposed current with high fidelity in regular tetrahedra. The best results occur where nonlinearities were constrained or eliminated (Dunlop et al., 2020). However, using actual spacecraft position data and a nonlinear magnetic environment, false currents were detected by the curlometer that were not imposed in the simulation. These false currents were produced while the quality parameter Q was within standard thresholds. Standing alone, this directly challenges the efficacy of Q but does not imply anything about the ring current itself. However, single perigee passes also displayed unique current structures. The strong hemispheric asymmetry of the current throughout the perigee passes, especially in the 2003 data where current components remained continuous without sudden spikes but diverged later in the flight track, casts doubt on the validity of the observed structure. These structures are contrary to plasma organization by magnetic field lines, which are oriented cross-hemisphere, and disagree with a pressure peak at low latitude. Although much of the divergent current region lies outside of $Q < 0.5$ and is therefore untrustworthy, the trends begin well within the filtered data. The diverging currents increase with tetrahedron irregularity, suggesting a causal relationship. In light of the simulated false currents, which also produce this divergence with tetrahedron irregularity, the single perigee passes all seem to contain some combination of poor tetrahedron quality or strong magnetic gradient that produces poor current estimates.

Radial and 3D plots of full current vectors combined from all perigee passes analyzed by curlometry are similarly unexpected. Currents are dominated by a large field-aligned component in both hemispheres at all local times that is southward and cross-equatorial. There is also a significant radial component Earthward at all local times. The most valuable product is azimuthal current as a function of L-shell, which produces a consistent value for quiet-time ring current below 10 nA/m^2 and hints at a current reversal to the eastward ring current within $L = 4$. Although less steep than anticipated, the curlometer does detect a radial current peak. Attempts to clarify and sharpen these analyses by restricting data to stable, trustworthy, or expected structure for individual perigee passes using established quality indices were unsuccessful in refining the dataset. Therefore, the ring current using Cluster data must stand as presented here, including the unusual features and limitations, and the confounding presence of false currents that greatly increase uncertainty.

Revisitation of Cluster ring current computation has called into question the efficacy of the curlometer technique in this region due to increased uncertainty. Individual time series plots show clear errors in current magnitude and direction, especially when the tetrahedron is distorted.

Furthermore, extensive simulation shows that the parameter Q does not always accurately represent the current estimate quality, and at the accepted threshold of $Q < 0.5$ can produce false currents as large as 100% of the actual current in complementary components. Lowering the threshold reduces the sample size to a highly-restricted domain that obscures sought trends. Previous current estimates of ~20 nA/m^2 are nevertheless not upheld by this study, with quiet cases overwhelmingly below 10 nA/m^2.

The discrepancy between legacy plasma moment estimates of ring current strength and distribution and Cluster curlometer values has narrowed significantly, with a newfound magnitude median peaking at just 7 nA/m^2. The new analysis presented above finds that the ring current is weaker during the 2002-2004 period than some previous curlometer estimates. Climatologies using these data should nevertheless be extremely cautious of the quality of current estimates, and effectively removing unsatisfactory cases reduces the sample size to preclude judgment on large-scale trends without removing the effects of false currents.

6. Conclusions

This study conducted a systematic assessment of current calculations using the curlometry technique in the inner magnetosphere, using the specific satellite alignments of the Cluster mission when it had a tetrahedral configuration at perigee. It was found that curlometry sometimes yields excellent reproductions of imposed currents, but other times produces large false currents due to the linearization within the calculation. The appearance of false currents is directly related to the orientation of the tetrahedron relative to the imposed current. Specifically, it was determined that larger false currents are produced when the largest planar semiaxis of the tetrahedron is more parallel to the local gradient of the magnetic field. These false currents can appear even when the elongation and planarity parameters signify only limited tetrahedron irregularity, and can be quite large even when the Q factor is below the nominally acceptable level of 0.5.

Keeping these limitations in mind, a statistical compilation of inner magnetospheric currents was then calculated. Although the new median ring current density of 7 nA/m^2 is in better agreement with other computation methods, there are still uncertainties associated with this measurement. The instrument magnetic field resolution alone introduces +/- 1.5 nA/m^2 of uncertainty (Vallat et al., 2005), and one must also consider the presence of false currents as an artifact of the nonlinearity. Even at $Q < 0.5$, these uncertainties can be quite large or even dominate the observed current structure, and are difficult to remove because of the complex dependence on tetrahedron orientation relative to the unknown currents. Furthermore, the interdependent nature of the curlometer current components necessitates the consideration of the large radial and field-aligned currents, which raise additional concerns due to unexpected structure.

Thus, any inner magnetospheric curlometry analysis that relies on Cluster ring current data, including magnitudes and climatologies, should be viewed with full knowledge of the caveats and limitations described herein. Although shortcomings in curlometry are discussed in detail here, the extent of this analysis is restricted to Cluster spacecraft within the specified orbits and around perigee. The use of curlometry elsewhere should be examined for similar effects, but the uncertainties in the ring current region cannot be directly applied to other regions because of the strong dependence on magnetic field nonlinearity and tetrahedron shape/orientation.

Acknowledgments and Data

This project was funded in part through a grant from the National Science Foundation's Research Experience for Undergraduates Program (Grant Number 1659248) and NSF grant 1663770, as well as by NASA grants 80NSSC17K0015 and NNX17AB87G. The authors give special thanks to the developers and curators of the SpacePy Python package, which proved invaluable for coordinate conversions and data processing. We would also like to acknowledge Dr. Michael Hirsch for use of his Python igrf12 package. DOI: 10.5281/zenodo.3461075. Cluster magnetometer data used in this study are available at the Cluster Science Archive (https://csa.esac.esa.int/csa-web/) and at NASA/GSFC's Space Physics Data Facility's CDAWeb service (https://cdaweb.gsfc.nasa.gov/), accessed October 2018. The simulated data sets and Python code are available at the University of Michigan Deep Blue data repository (https://deepblue.lib.umich.edu/data). We will "mint a DOI" to finalize and freeze the data brick upon acceptance.

References

Alken, P., Thébault, E., Beggan, C. D., Amit, H., Aubert, J., Baerenzung, J., et al. (2021). International Geomagnetic Reference Field: the thirteenth generation. *Earth, Planets and Space*, 73, 49. https://doi.org/10.1186/s40623-020-01288-x

Balogh, A., Dunlop, M. W., Cowley, S. W. H., Southwood, D. J., Thomlinson, J. G., Glassmeier, K. H., et al. (1997). The Cluster Magnetic Field Investigation. *Space Science Reviews*, 79**,** 65–91. https://doi.org/10.1023/A:1004970907748

Balogh, A., Carr, C. M., Acuña, M. H., Dunlop, M. W., Beek, T. J., Brown, P., et al. (2001). The Cluster Magnetic Field Investigation: overview of in-flight performance and initial results. *Annales Geophysicae*, 19(10/12), 1207–1217. https://doi.org/10.5194/angeo-19-1207-2001.

Daly, P. W., & Kronberg, E. A. (2013). User Guide to the RAPID Measurements in the Cluster Science Archive (CSA) (5.4). Goettingen, Germany.

Dandouras, I., & Barthe, A. (2011). User Guide to the CIS measurements in the Cluster Active Archive (CAA) (Vol. 2.0).

Dandouras, I., & Barthe, A. (2015). Cluster Active Archive: Interface Control Document for CIS.

Dandouras, I., Rochel-Grimald, S., Vallat, C., & Dunlop, M. W. (2018). Terrestrial ring current: A review of Cluster results based on the curlometer technique. *Electric Currents in Geospace and Beyond*. https://doi.org/10.1002/9781119324522.ch7.

Dunlop, M. W., Balogh, A., Glassmeier, K.-H., & Robert, P. (2002). Four-point Cluster application of magnetic field analysis tools: The Curlometer. *Journal of Geophysical Research*, 107, 1384. DOI:10.1029/2001JA005088.

Dunlop, M. W., Haaland, S., Dong, X. C., Middleton, H. R., Escoubet, C. P., Yang, Y. Y., et al. (2018). Multipoint analysis of electric currents in geospace using the curlometer technique. *Electric Currents in Geospace and Beyond*, 67–80. https://doi.org/10.1002/9781119324522.ch4.

Dunlop, M. W., Haaland, S., Escoubet, P. C., & Dong, X.-C. (2016). Commentary on accessing 3-D currents in space: Experiences from Cluster. *Journal of Geophysical Research: Space Physics*, 121(8), 7881–7886. https://doi.org/10.1002/2016JA022668.

Dunlop, M. W., Southwood, D. J., Glassmeier, K. H., & Neubauer, F. M. (1988). Analysis of multipoint magnetometer data. *Advances in Space Research*, 8(9–10), 273–277. https://doi.org/10.1016/0273-1177(88)90141-X.

Dunlop M.W., Yang J.Y., Yang Y.Y., Lühr H., Cao J.B. (2020). Multi-spacecraft Current Estimates at Swarm. In: Dunlop M., Lühr H. (eds) Ionospheric Multi-Spacecraft Analysis Tools. ISSI Scientific Report Series, vol 17. Springer, Cham. https://doi.org/10.1007/978-3-030-26732-2_5

Dunlop, M. W., Yang, J. Y., Yang, Y. Y., Xiong, C., Lühr, H., Bogdanova, Y. V., et. al (2015). Simultaneous field-aligned currents at Swarm and Cluster satellites. *Geophysical Research Letters*, 42(10), 3683–3691. https://doi.org/10.1002/2015GL063738.

Fränz, M., & Harper, D. (2002). Heliospheric coordinate systems. *Planetary and Space Science*, 50(2), 217–233. https://doi.org/10.1016/S0032-0633(01)00119-2.

Ganushkina, N. Y., Liemohn, M. W., Dubyagin, S., Daglis, I. A., Dandouras, I., DeZeeuw, D. L, et. al (2015). Defining and resolving current systems in geospace. *Annales Geophysicae*, 33, 1269-1402. doi:10.5194/angeo-33-1369-2015

Ganushkina, N. Y., Liemohn, M. W., & Dubyagin, S. (2018), Current systems in the Earth's magnetosphere, *Reviews of Geophysics*, *56*(2), 309-332, doi: 10.1002/2017RG000590.

Greenspan, M. E., & Hamilton, D. C. (2000). A test of the Dessler-Parker-Sckopke relation during magnetic storms. *Journal of Geophysical Research Space Physics*, *105*, 5419-5430.

Grimald, S., Dandouras, I., Robert, P., & Lucek, E. (2012). Study of the applicability of the curlometer technique with the four Cluster spacecraft in regions close to Earth. *Annales Geophysicae*, 30(3), 597–611. https://doi.org/10.5194/angeo-30-597-2012.

Hapgood, M. A. (1992). Space physics coordinate transformations: A user guide. Planetary and Space Science, 40(5), 711–717. https://doi.org/10.1016/0032-0633(92)90012-D.

Henderson, P. D., Owen, C. J., Lahiff, A. D., Alexeev, I. V., Fazakerley, A. N., Yin, L., et al. (2008). The relationship between j × B and ∇·Pe in the magnetotail plasma sheet: Cluster observations. *Journal of Geophysical Research: Space Physics*, 113(7), 1–17. https://doi.org/10.1029/2007JA012697.

Laakso, H., Perry, C., McCaffrey, S., Herment, D., Allen, A. J., Harvey, C. C., et al. (2010). Cluster Active Archive: Overview. In H. Laakso et al. (Ed.), *Astrophysics and Space Science Proceedings* (pp. 3–37).

Le, G., Russell, C. T., & Takahashi, K. (2004). Morphology of the ring current derived from magnetic field observations. *Annales Geophysicae*, 22, 1267-1295. 10.5194/angeo-22-1267-2004.

Liemohn, M. W., Kozyra, J. U., Thomsen, M. F., Roeder, J. L., Lu, G., Borovsky, J. E., & Cayton, T. E. (2001). Dominant role of the asymmetric ring current in producing the stormtime Dst*, *Journal of Geophysical Research*, 106, 10883-10904. DOI:10.1029/2000JA000326.

Liemohn, M. W., Kozyra, J. U., Clauer, C. R., & Ridley, A. J. (2001). Computational analysis of the near-Earth magnetospheric current system, *Journal of Geophysical Research*, 106, 29,531, 2001. DOI: 10.1029/2001JA000045.

Liemohn, M. W., Katus, R. M., & Ilie, R. (2015), Statistical analysis of storm-time near-Earth current systems, *Annales Geophysicae, 33*, 965-982, doi: 10.5194/angeo-33-965-2015.

Liemohn, M. W., Ganushkina, N. Y., Ilie, R., & Welling, D. T. (2016). Challenges associated with near-Earth nightside current. *Journal of Geophysical Research: Space Physics*, 121, 6763–6768. https://doi.org/10.1002/2016JA022948.

Lui, A. T. Y., & Hamilton, D. C. (1992). Radial profiles of quiet time magnetospheric parameters. *Journal of Geophysical Research*, 97(A12), 19325. https://doi.org/10.1029/92ja01539.

Lui, A. T. Y., McEntire, R.W., & Krimigis, S. M. (1987). Evolution of the ring current during two geomagnetic storms. *Journal of Geophysical Research*, 92, 7459–7470.

Middleton, H., & Masson, A. (2016). The Curlometer technique: a beginner's guide. ESDC-CSA-TN-0001 (Vol. 1).

Milillo, A., Orsini, S., & Daglis, I. A. (2001). Empirical model of proton fluxes in the equatorial inner magnetosphere: Development. *Journal of Geophysical Research Space Physics, 106*, 25,713-25,729.

Milillo, A., Orsini, S., Delacourt, D. C., Mura, A., Massetti, S., De Angelis, E., & Ebihara, Y. (2003), Empirical model of proton fluxes in the equatorial inner magnetosphere: 2. Properties and applications, *Journal of Geophysical Research Space Physics*, 108, A5. 1165// https://doi.org/10.1029/2002JA009581

Morley, S., Koller, J., Welling, D., Larsen, B., Henderson, M., & Niehof, J. (2011). "Spacepy - A Python-based library of tools for the space sciences". In "*Proceedings of the 9th Python in science conference (SciPy 2010)*".

Paschmann, G., & Daly, P. W. (2000). Analysis Methods for Multi-Spacecraft Data. ISSI Scientific Report.

Petrukovich, A., Artemyev, A., Vasko, I., Nakamura, R., & Zelenyi, L. (2015). Current Sheets in the Earth Magnetotail: Plasma and Magnetic Field Structure with Cluster Project Observations. *Space Science Reviews*, 188(1–4), 311–337. https://doi.org/10.1007/s11214-014-0126-7.

Reme, H., Bosqued, J. M., Sauvaud, J. A., Cros, A., Dandouras, J., Aoustin, C., et al. (1997). The Cluster Ion Spectrometry (CIS) Experiment. *Space Science Reviews*, 79, 303–350. Retrieved from http://www.space.irfu.se/exjobb/2003_erik_bergman/articles/CIS.pdf

Robert, P., Dunlop, M. W., Roux, A., & Chanteur, G. (1998). Reprinted from Analysis Methods for Multi-Spacecraft Data Accuracy of Current Density Determination 16.1 Introduction. In G. Paschmann & P. W. Daly (Eds.), Analysis Methods for Multi-Spacecraft Data (1.1, pp. 395–418). ISSI/ESA.

Sergis, N., Krimigis, S. M., Mitchell, D. G., Hamilton, D. C., Krupp, N., Mauk, B. M., et al. (2007). Ring current at Saturn: Energetic particle pressure in Saturn's equatorial magnetosphere measured with Cassini/MIMI. *Geophysical Research Letters*, 34(9), 1–6. https://doi.org/10.1029/2006GL029223.

Shen, C., Yang, Y. Y., Rong, Z. J., Li, X., Dunlop, M., Carr, C. M., et al. (2014). Direct calculation of the ring current distribution and magnetic structure seen by Cluster during geomagnetic storms. *Journal of Geophysical Research: Space Physics*, 119(4), 2458–2465. https://doi.org/10.1002/2013JA019460.

Vallat, C., Dandouras, I., Dunlop, M., Balogh, A., Lucek, E., Parks, G. K., et al. (2005). First current density measurements in the ring current region using simultaneous multi-spacecraft CLUSTER-FGM data. *Annales Geophysicae*, 23(5), 1849–1865. https://doi.org/10.5194/angeo-23-1849-2005.

Zhang, Q. H., Dunlop, M. W., Lockwood, M., Holme, R., Kamide, Y., Baumjohann, W., et al. (2011). The distribution of the ring current: Cluster observations. *Annales Geophysicae*, 29(9), 1655–1662. https://doi.org/10.5194/angeo-29-1655-2011.

Journal of Geophysical Research - Space Physics

Supporting Information for

Cluster Curlometry Limitations in the Ring Current Region

T. B. Keebler[1], M. W. Liemohn[1], N. Y. Ganushkina[1,2]

[1] Department of Climate and Space Sciences and Engineering, University of Michigan, Ann Arbor, MI.

[2] Space Research and Observation Technologies, Space and Earth Observation Centre, Finnish Meteorological Institute, Helsinki, Finland

Contents of this file

Figures S1 to S20

Additional Supporting Information (Files uploaded separately)

Captions for Movies S1 to S2

Introduction

The plots and animations herein supplement the material in the article by providing enhanced visualization and additional method verification. The first set of figures verify the correct operation of the curlometer script used for this study. Be careful to note that both vertical and horizontal axes are scaled to show detail and are not necessarily the same for comparable plots. These are followed by plots to be compared directly with selected figures from previous studies, with detailed descriptions of the differences in computation and generation. Finally, two animations are provided for cases involving the tetrahedron rotation and the generation of false currents. These animations add clarity to a complex process that is difficult to represent in stationary plots. The animation files are in the GIF format.

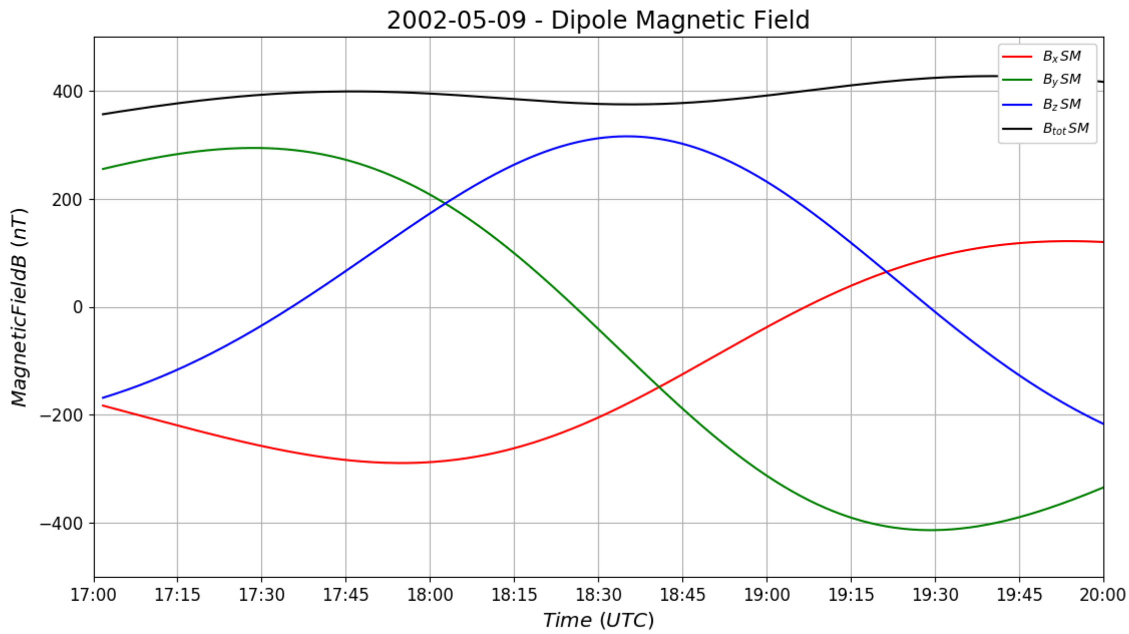

Figure S1. 9 May 2002 perigee pass with magnetometer data replaced by a simple approximation of Earth's dipole field.

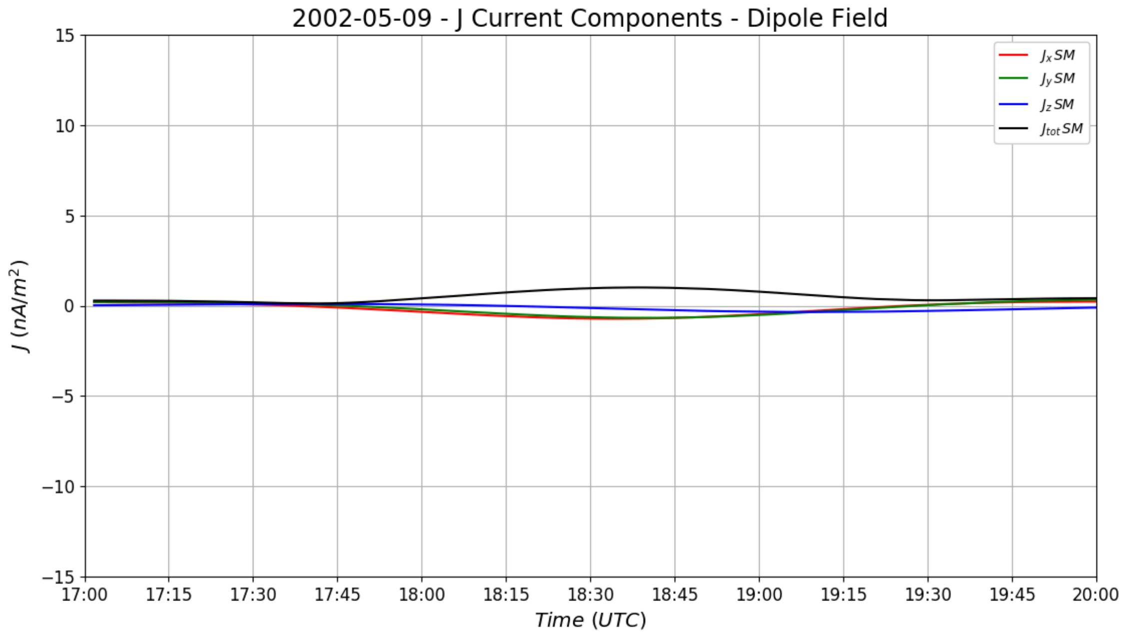

Figure S2. Curlometer currents output from the 9 May 2002 perigee pass with magnetometer data replaced by a simple approximation of Earth's dipole field.

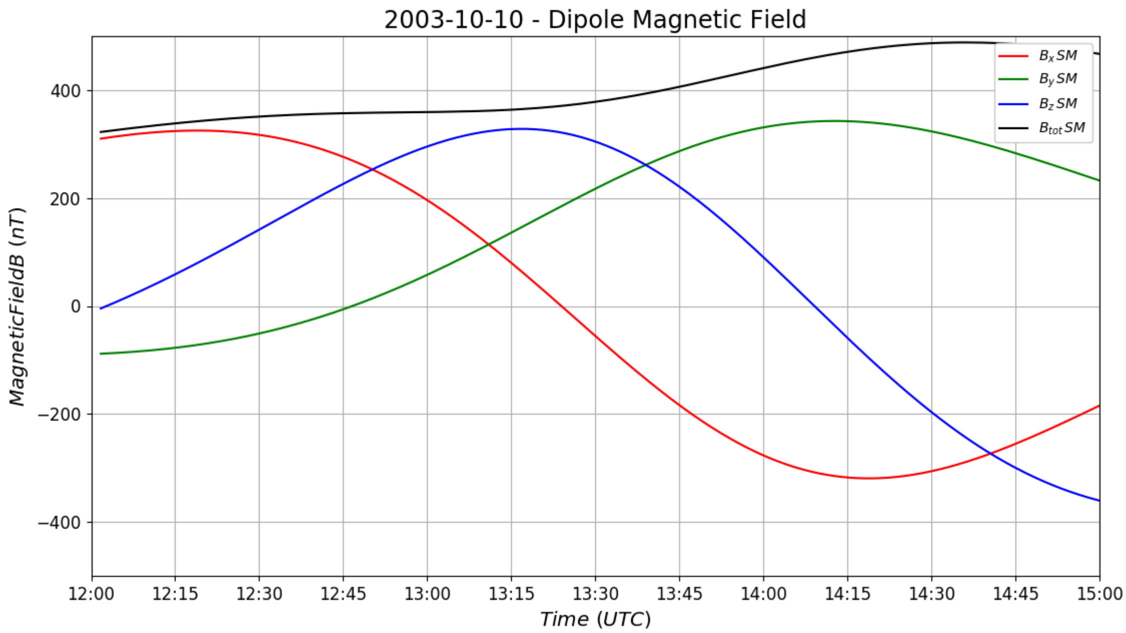

Figure S3. 10 October 2003 perigee pass with magnetometer data replaced by a simple approximation of Earth's dipole field.

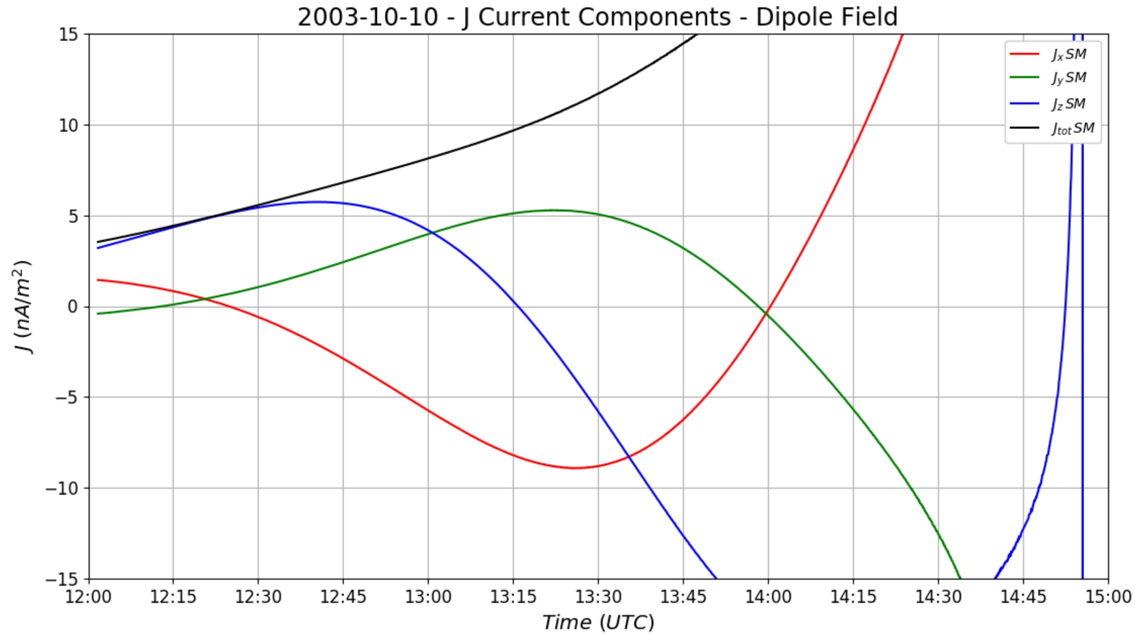

Figure S4. Curlometer currents output from the 10 October 2003 perigee pass with magnetometer data replaced by a simple approximation of Earth's dipole field.

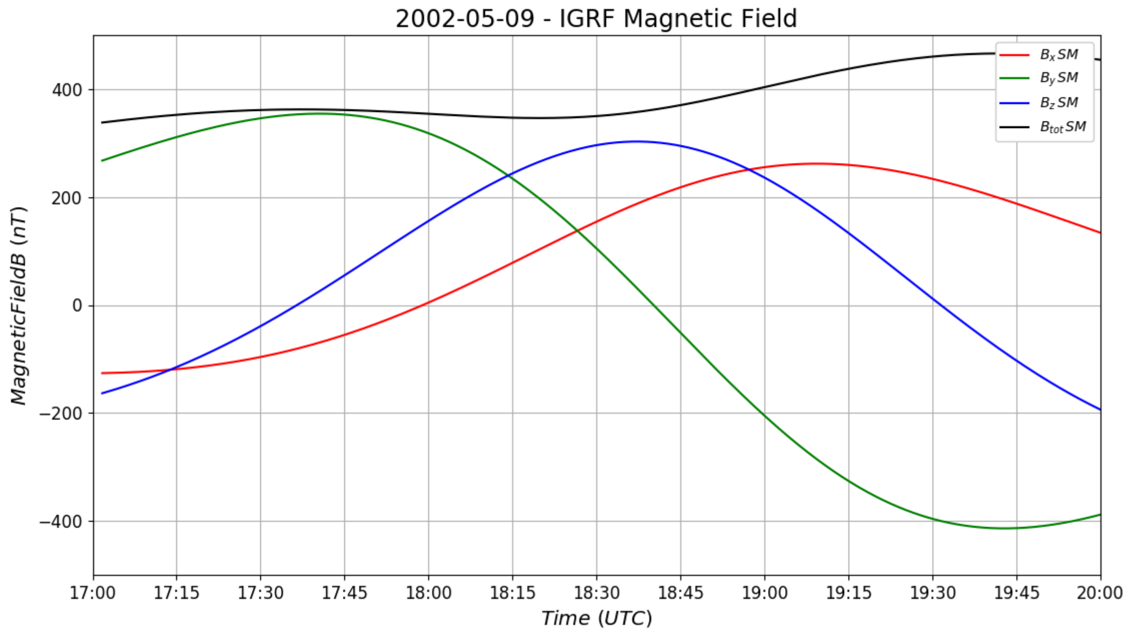

Figure S5. 9 May 2002 perigee pass with magnetometer data replaced by the International Geomagnetic Reference Field (IGRF) magnetic environment.

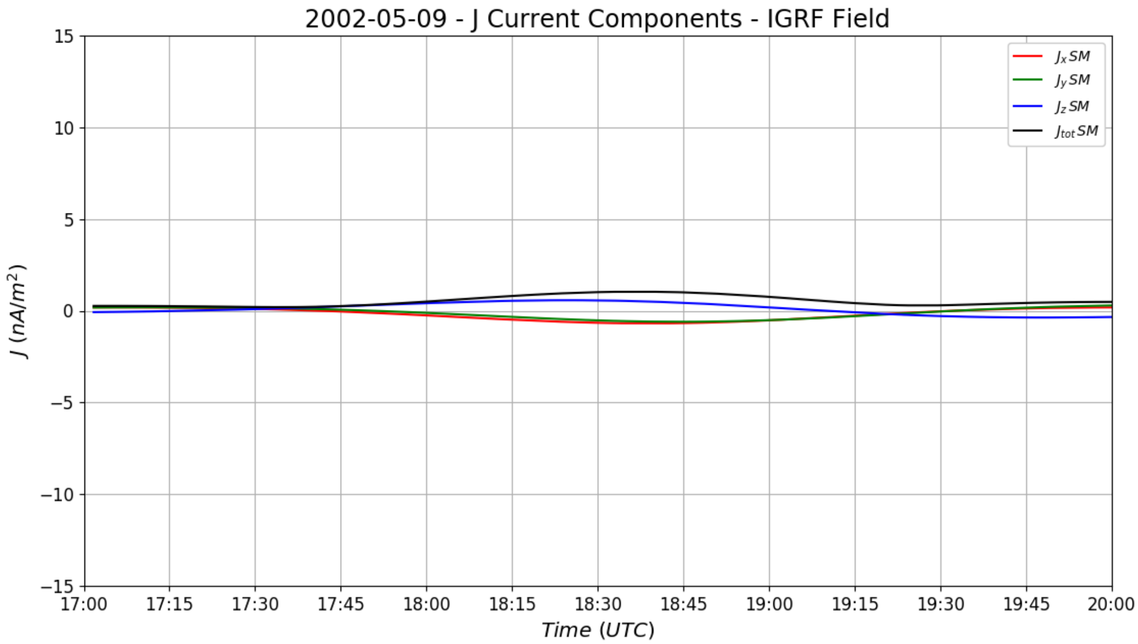

Figure S6. Curlometer currents output from the 9 May 2002 perigee pass with magnetometer data replaced by the IGRF magnetic environment.

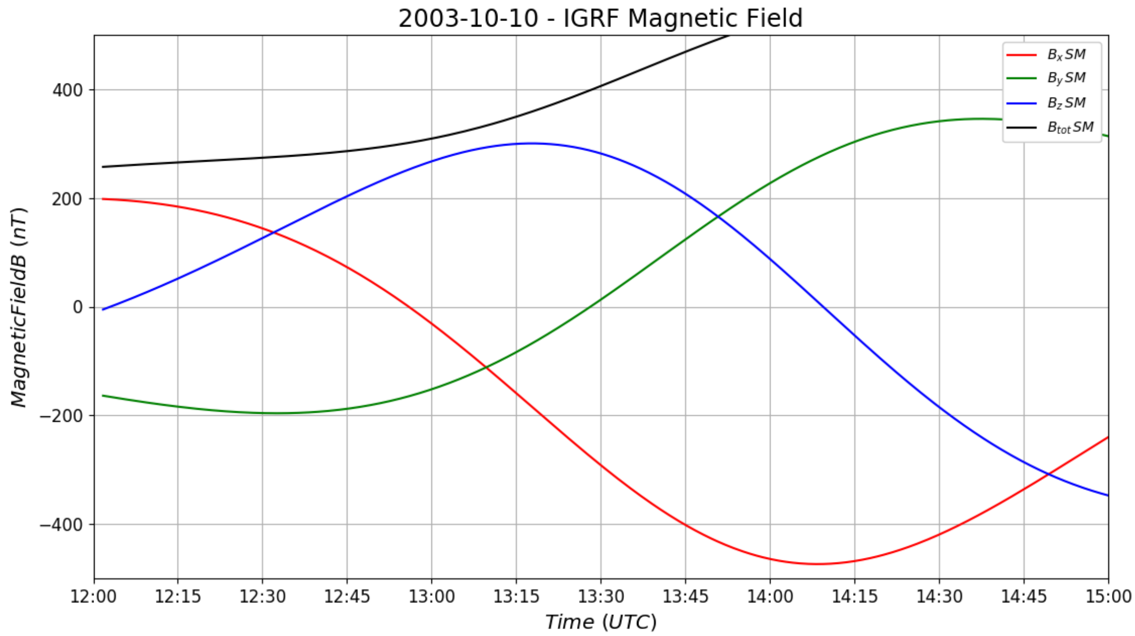

Figure S7. 10 October 2003 perigee pass with magnetometer data replaced by the IGRF magnetic environment.

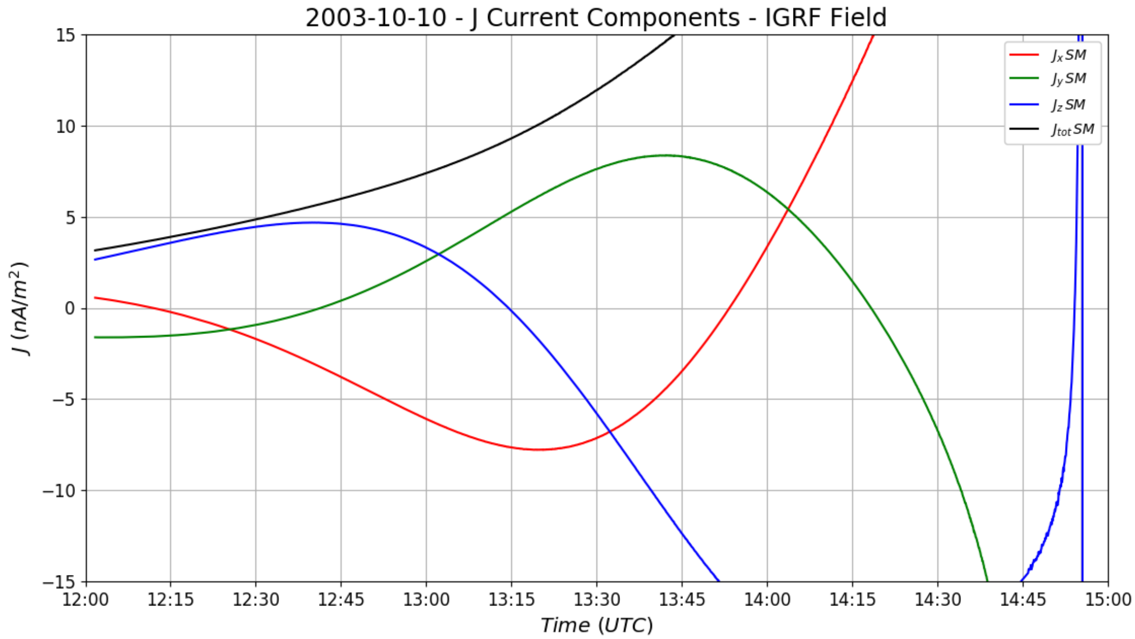

Figure S8. Curlometer currents output from the 10 October 2003 perigee pass with magnetometer data replaced by the IGRF magnetic environment.

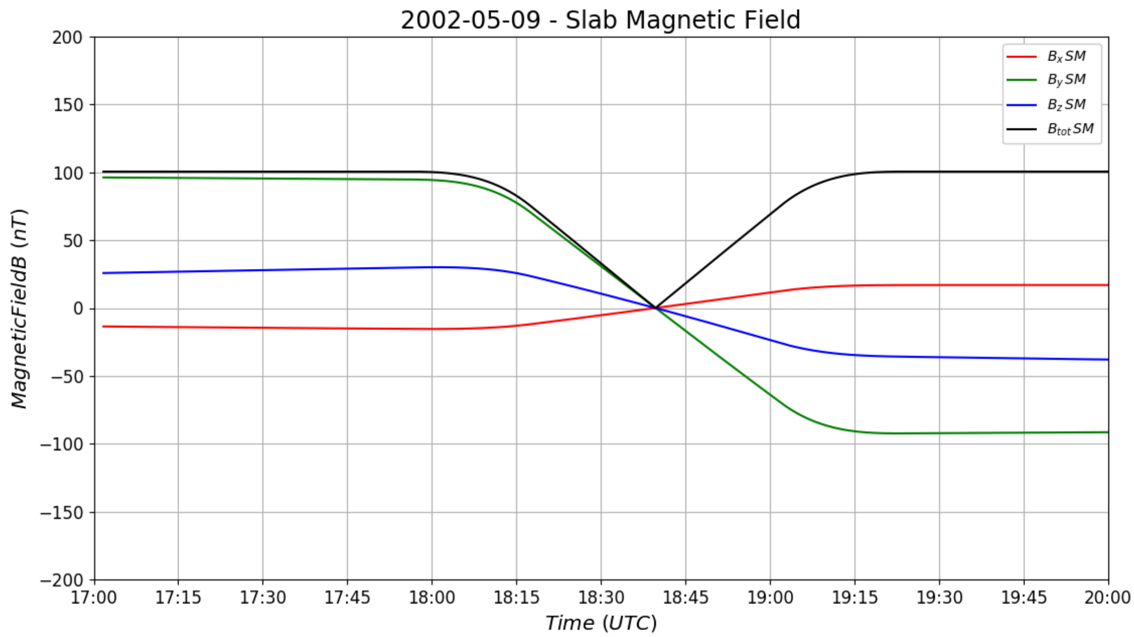

Figure S9. 9 May 2002 perigee pass with magnetometer data replaced by a simulated infinite current sheet (slab) in the z = 0 plane. The simulated slab current is constant over a finite thickness larger than the tetrahedron size, and tapers quadratically to either side.

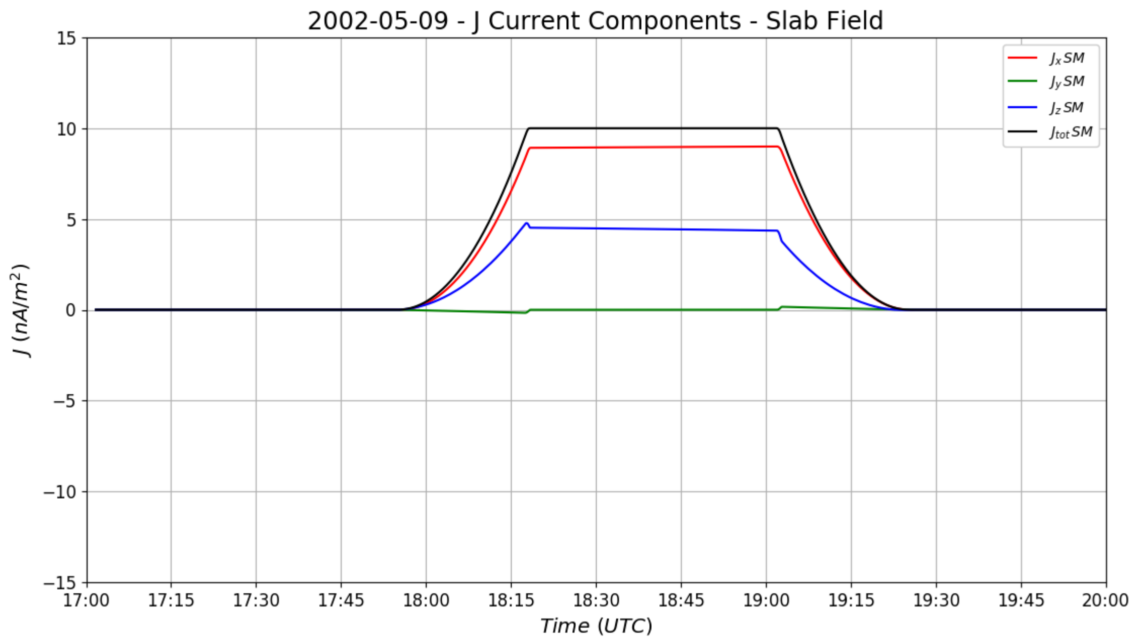

Figure S10. Curlometer currents output from the 9 May 2002 perigee pass with magnetometer data replaced by a simulated infinite current sheet in the z = 0 plane. The simulated slab current is constant over a finite thickness larger than the tetrahedron size, and tapers quadratically to either side. Note that the black current captures the imposed simulation current almost perfectly at 10 nA/m^2.

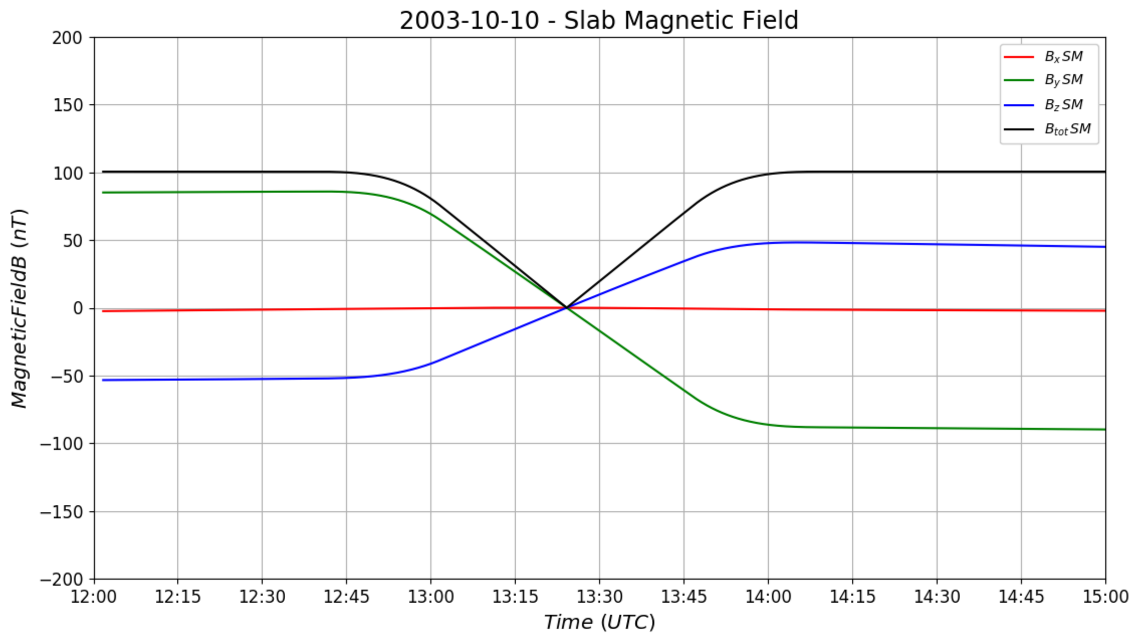

Figure S11. 10 October 2003 perigee pass with magnetometer data replaced by a simulated infinite current sheet (slab) in the z = 0 plane. The simulated slab current is constant over a finite thickness larger than the tetrahedron size, and tapers quadratically to either side.

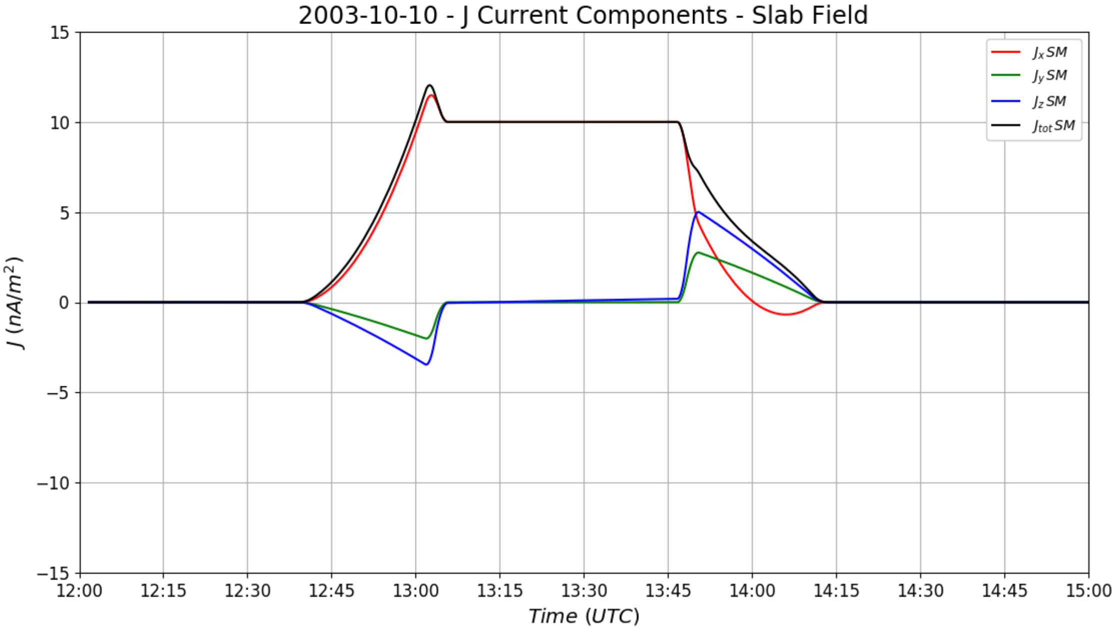

Figure S12. Curlometer currents output from the 10 October 2003 perigee pass with magnetometer data replaced by a simulated infinite current sheet in the z = 0 plane. The simulated slab current is constant over a finite thickness larger than the tetrahedron size, and tapers quadratically to either side. Note that the black current captures the imposed simulation current almost perfectly at 10 nA/m^2. Also note that, while in the sharp gradients to either side, the curlometer technique becomes inaccurate in all components.

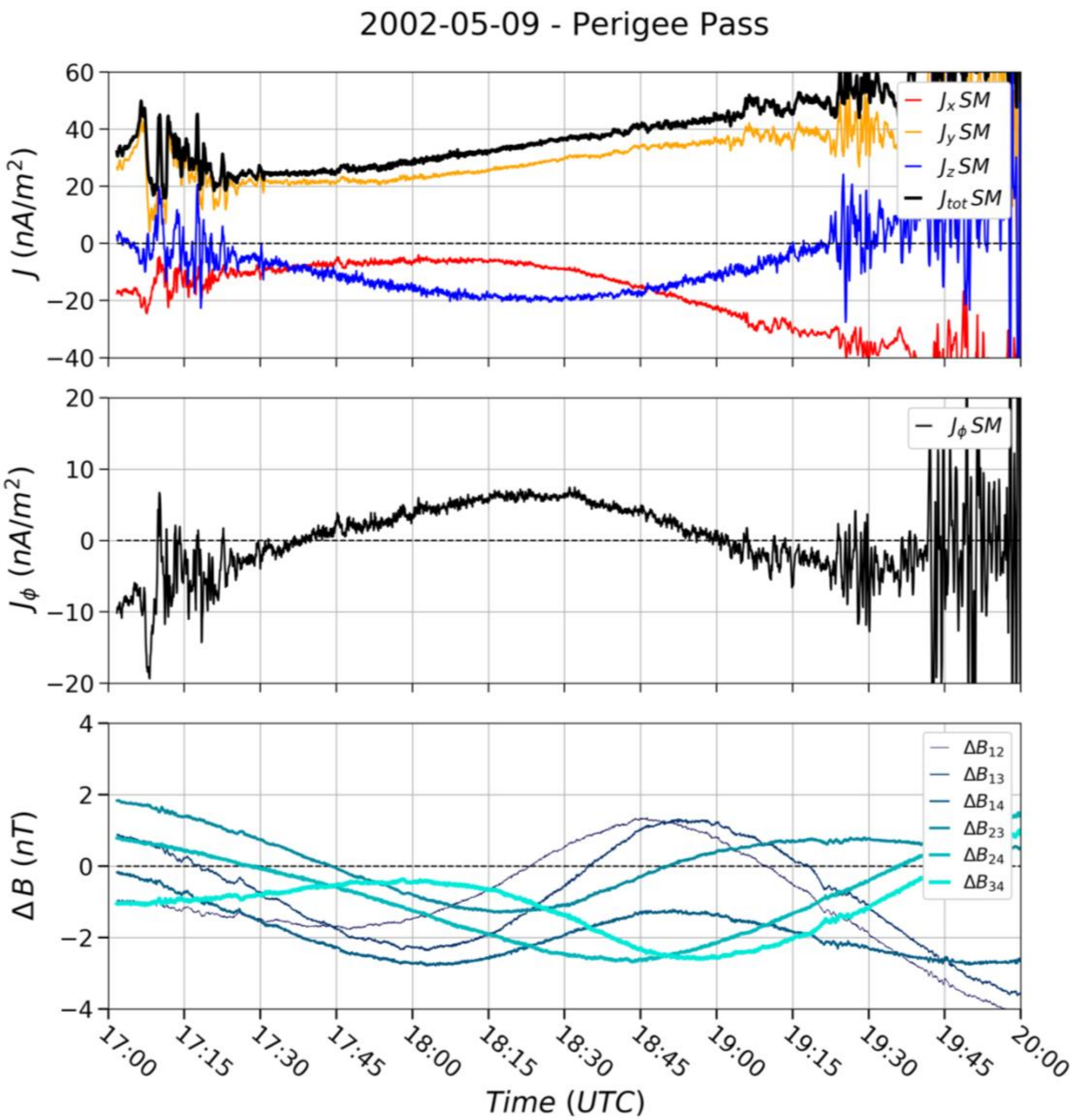

Figure S13. Investigation of instrument sensitivity for Cluster tetrahedron. Using the 9 May 2002 perigee pass, the magnetometer resolution of 0.125 nT was subtracted uniformly in time from the Cluster 1 spacecraft, chosen as the most irregular in the direction of the gradient for largest effect. The curlometer output of the modified magnetic data showed a decrease of about 2 nT in the azimuthal current. Compare Figure S13 to Figure S14, Figure S15, and Figure 1 in the paper.

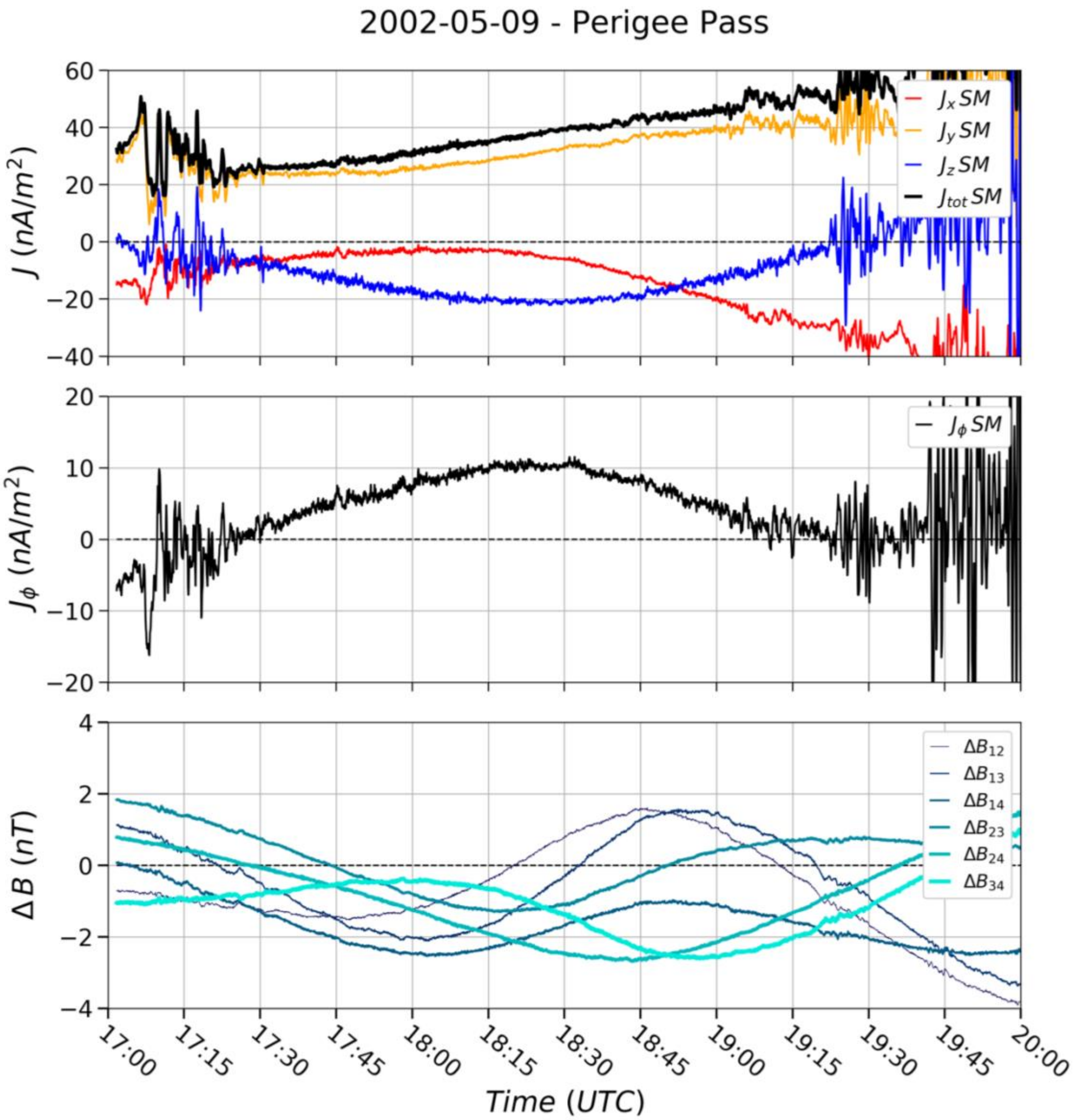

Figure S14. Investigation of instrument sensitivity for Cluster tetrahedron. Using the 9 May 2002 perigee pass, the magnetometer resolution of 0.125 nT was added uniformly in time from the Cluster 1 spacecraft, chosen as the most irregular in the direction of the gradient for largest effect. The curlometer output of the modified magnetic data showed an increase of about 1 nT in the azimuthal current. Compare Figure S14 to Figure S13, Figure S15, and Figure 1 in the paper.

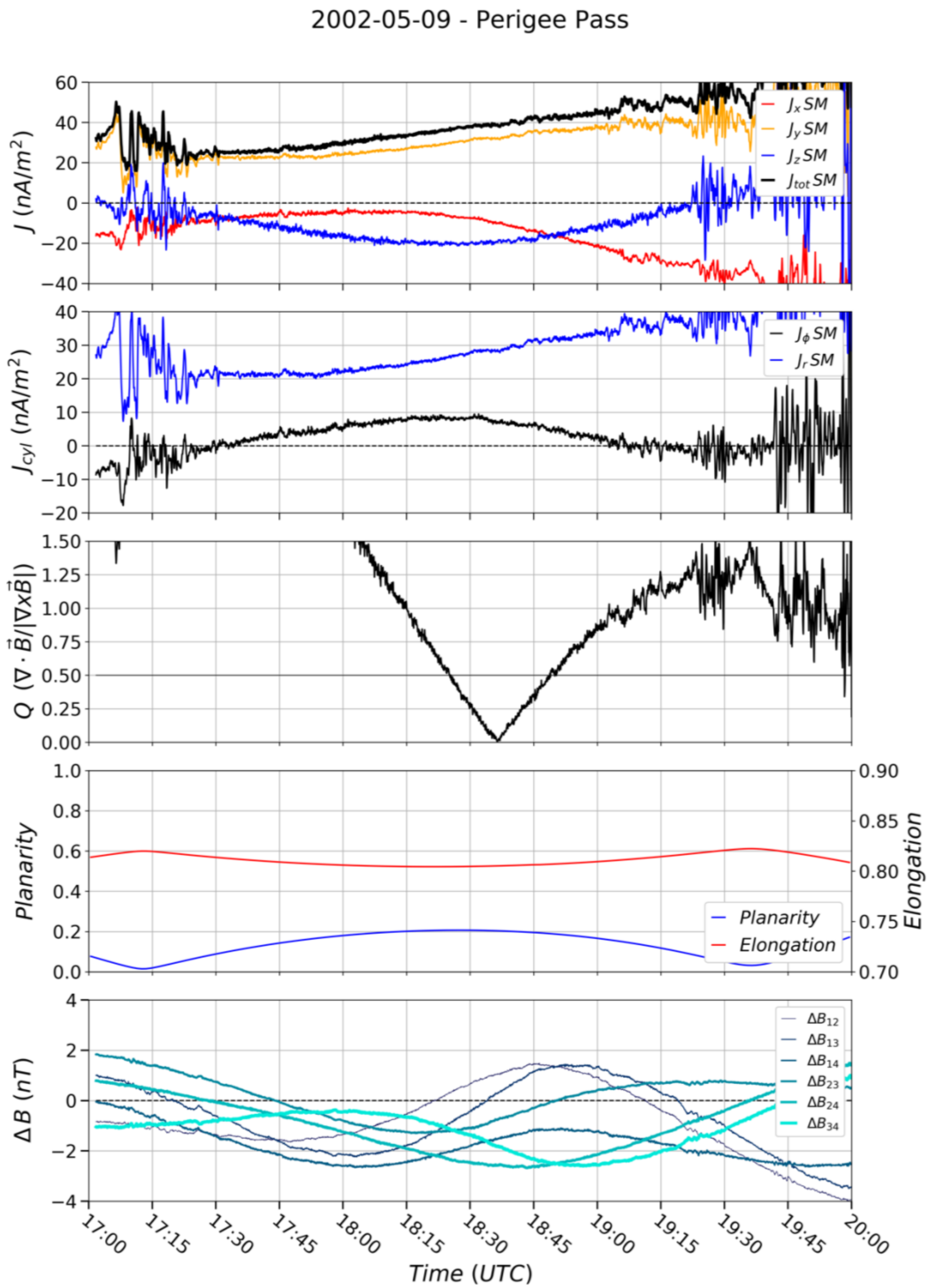

Figure S15. Full parameter consideration for the 9 May 2002 perigee pass. The panels from top to bottom depict:

- Cartesian and total currents in SM coordinates
- Azimuthal and radial current components in SM/local cylindrical coordinates
- Tetrahedron quality parameter Q

- Tetrahedron geometry factors elongation (E) and planarity (P)
- Magnetic field differences between spacecraft pairs

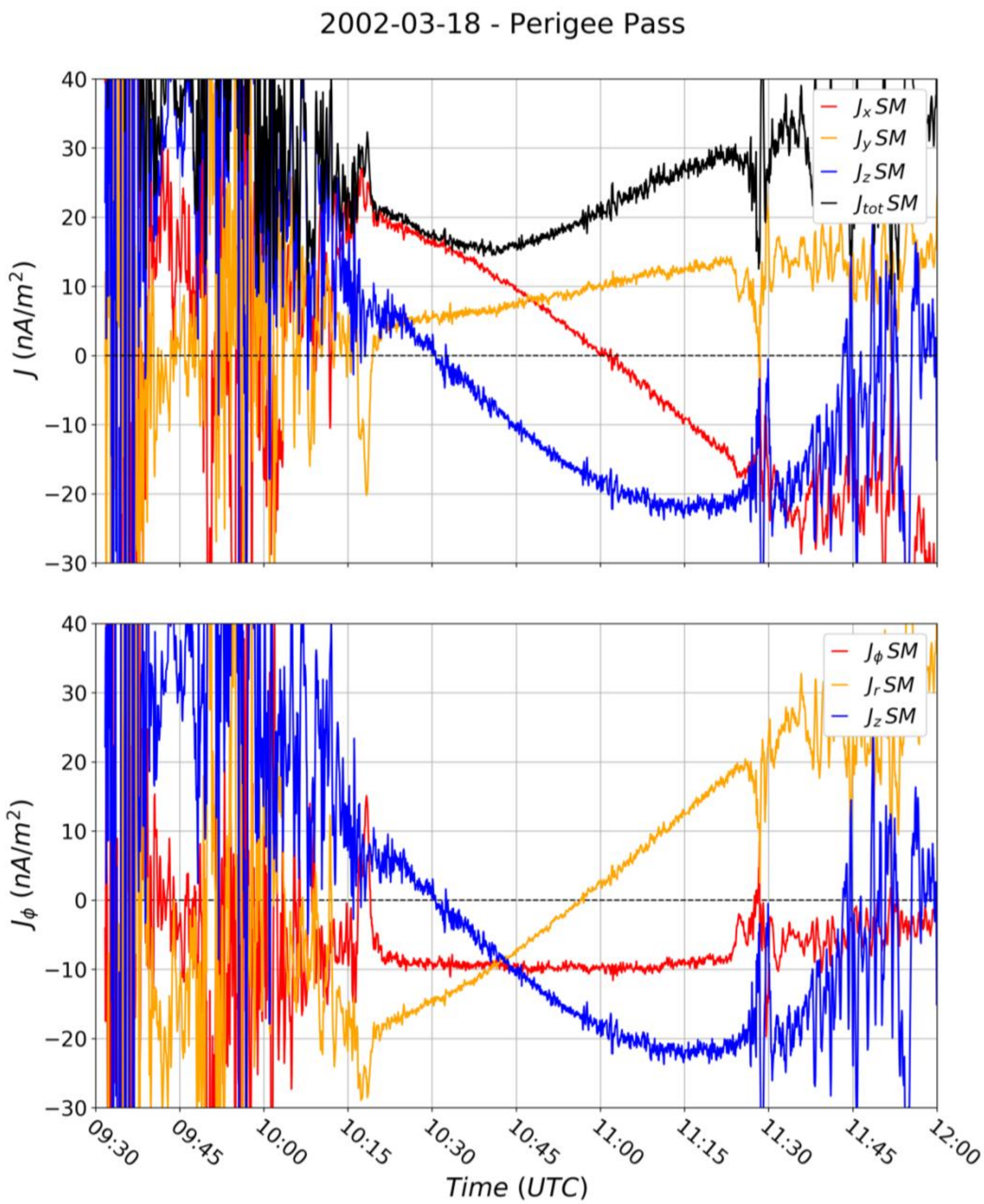

Figure S16. Curlometer currents output from the 18 March 2002 perigee pass. This figure is constructed in the same manner as Figure 9 in Vallat et al. (2005). Note that this figure has the signs of some components reversed to match the convention used in that paper.

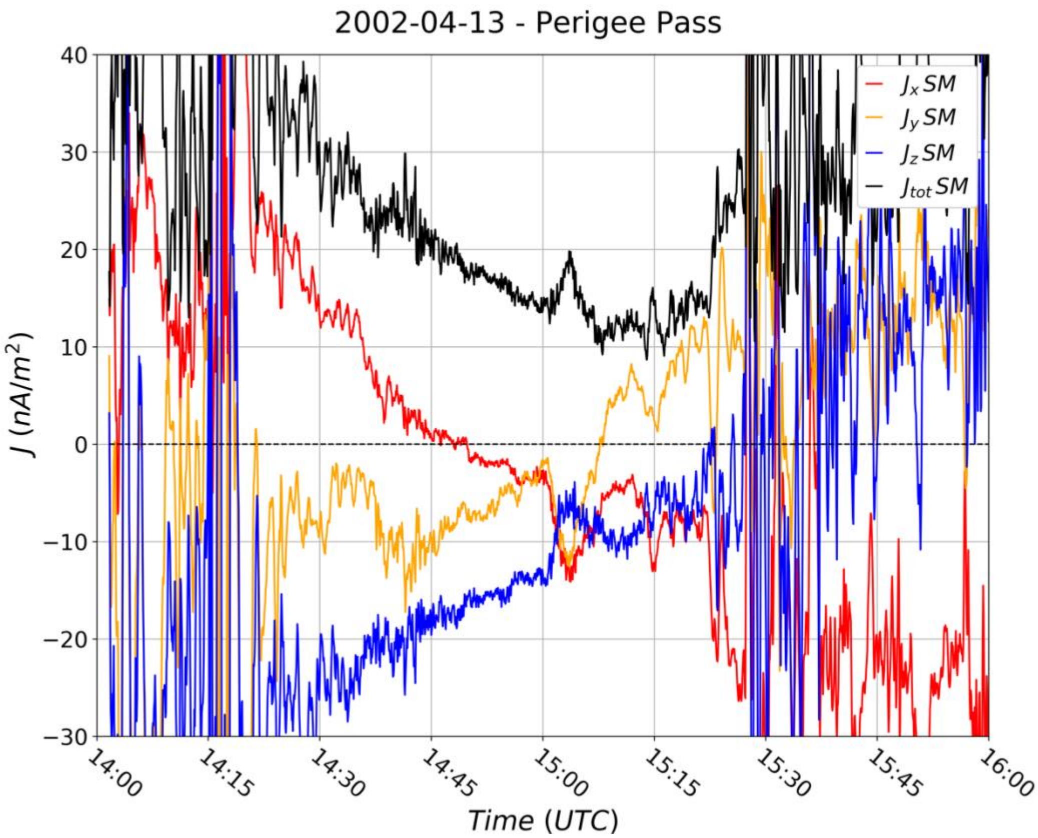

Figure S17. Curlometer currents output from the 13 April 2002 perigee pass. This figure is constructed in the same manner as Figure 2 in Vallat et al. (2005). Note that this figure has the signs of some components reversed to match the convention used in that paper.

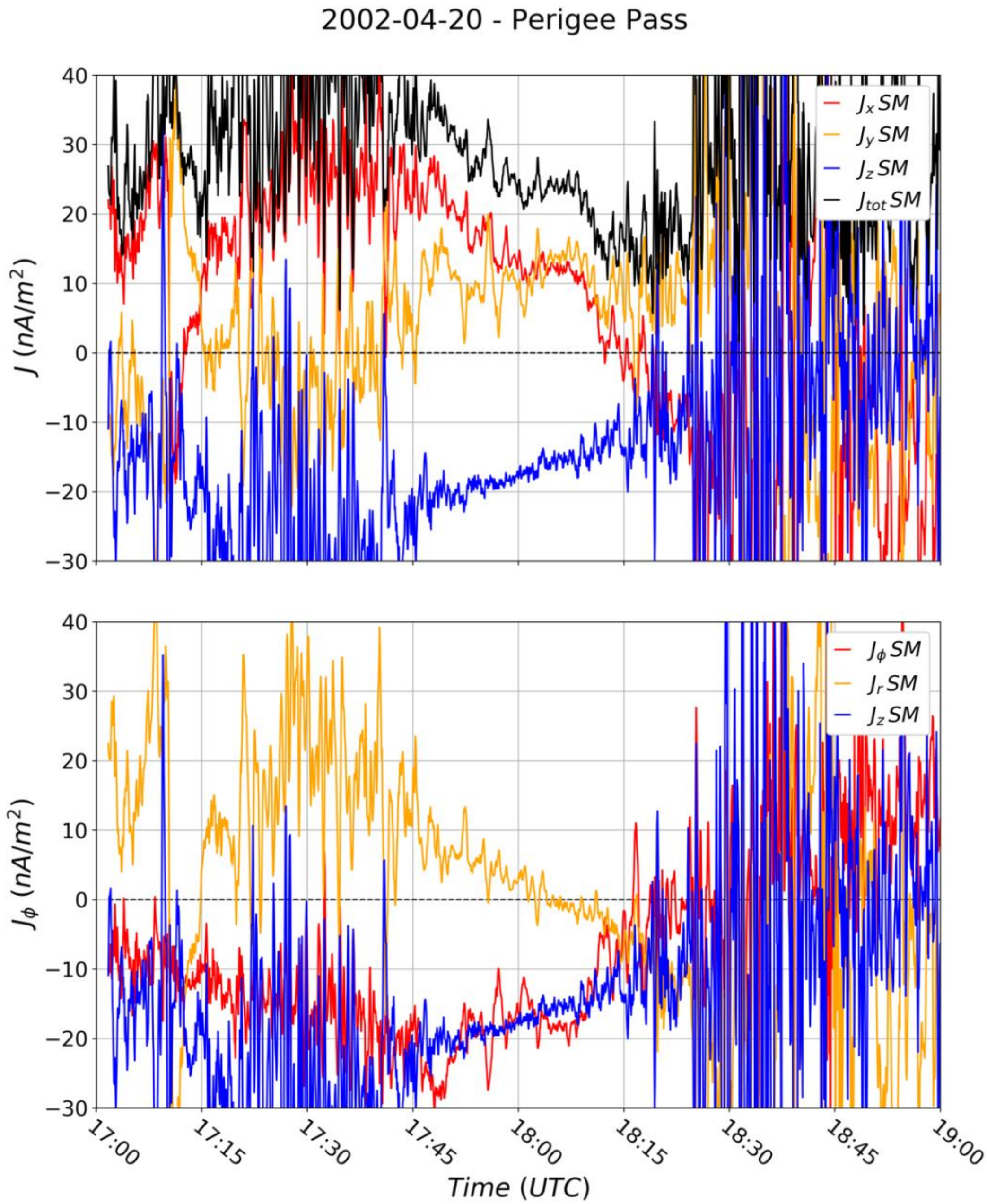

Figure S18. Curlometer currents output from the 20 April 2002 perigee pass. This figure is constructed in the same manner as Figure 14 in Vallat et al. (2005). Note that this figure has the signs of some components reversed to match the convention used in that paper.

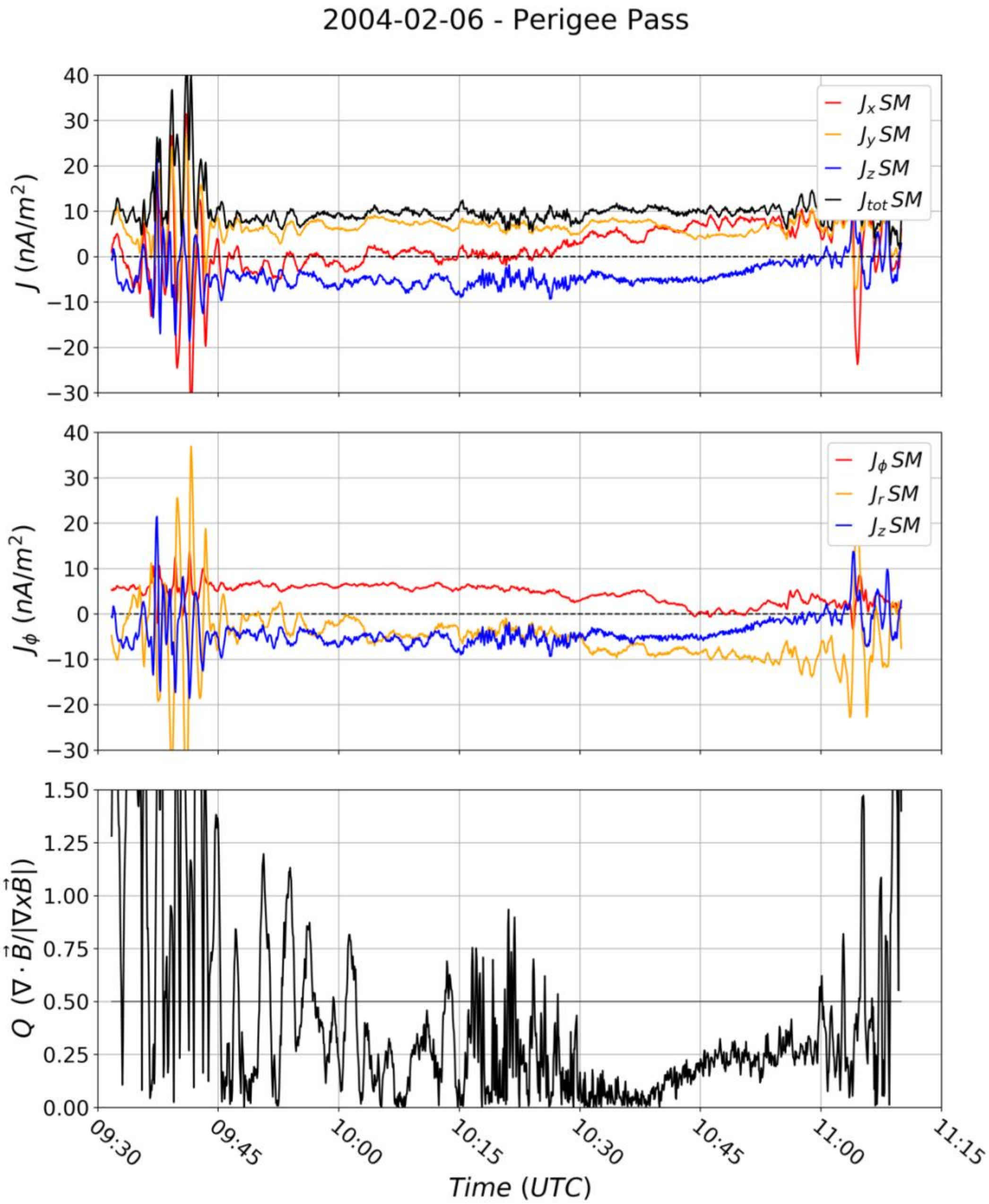

Figure S19. Curlometer currents output from the 6 February 2004 perigee pass. This figure is constructed in the same manner as Figure 2 in Zhang et al. (2011).

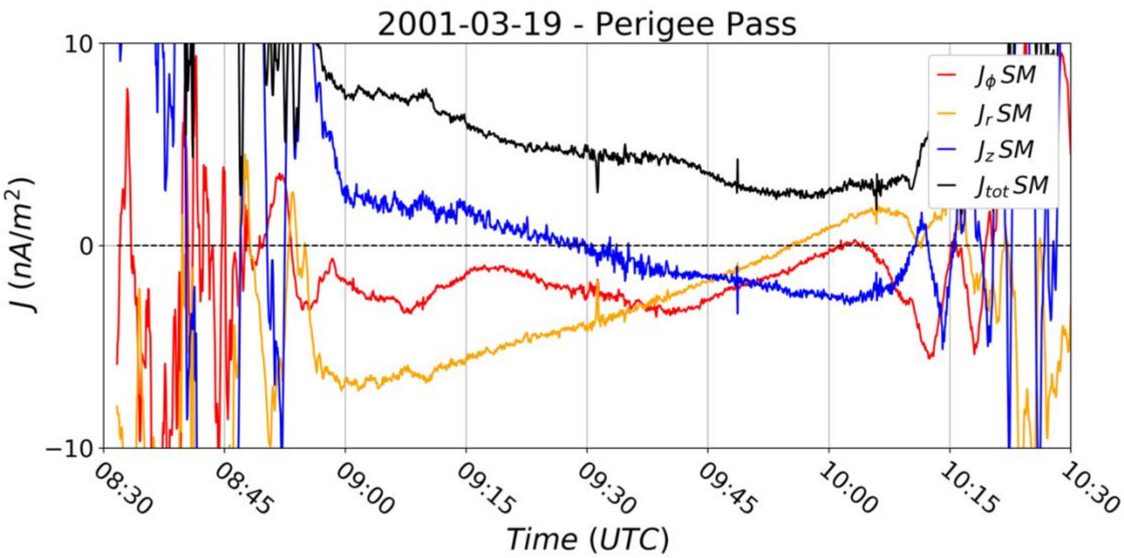

Figure S20. Curlometer currents output from the 19 March 2001 perigee pass. This figure is constructed in the same manner as Figure 9 in Shen et al. (2014).

Movie S1. Tetrahedron rotation for the 10 October 2003 perigee pass. This animation shows rotation of all spacecraft together around the tetrahedron barycenter, and the effect on curlometer output of a simulated current environment. Note that, depending on orientation with respect to a stationary current structure and magnetic topology, the exact same tetrahedron shape and size can produce very different current outputs. Two still frames from this animation are provided in the paper as Figure 4, to highlight the extrema of the animation.

Movie S2. Tetrahedron rotation for the 18 March 2002 perigee pass. This animation shows rotation of all spacecraft together around the tetrahedron barycenter, and the effect on curlometer output of a simulated current environment. Contrary to Movie S1, this event is from 2002, which has a much smaller tetrahedron size. Thus, in the exact same simulated current sheet, the smaller tetrahedron does not produce a large false current at any rotation. However, events from this timeframe make up a small subset of the existing curlometer analysis in the literature.